

Far-infrared Polarization Properties of Nearby Star-forming Regions: A New Compendium of SOFIA/HAWC+ Observations

KAITLYN KARPOVICH ^{1,2} SUSAN E. CLARK ^{1,2} AND ENRIQUE LOPEZ-RODRIGUEZ ³

¹*Department of Physics, Stanford University, Stanford, CA 94305, USA*

²*Kavli Institute for Particle Astrophysics & Cosmology (KIPAC), Stanford University, Stanford, CA 94305, USA*

³*Department of Physics & Astronomy, University of South Carolina, Columbia, SC 29208, USA*

ABSTRACT

We present a comprehensive polarimetric study of 26 nearby molecular clouds in four far-infrared bands (53 μm to 214 μm) using 52 archival SOFIA/HAWC+ datasets. Far-infrared dust polarization observations probe the plane-of-sky magnetic field. To investigate scale-dependent trends, we group the molecular clouds by distance and analyze the data at common angular (25'') and common physical (0.052 pc and 0.32 pc) resolutions. The two shorter wavelengths are more impacted by smoothing, exhibiting a larger decrease in percent polarization. We analyze the polarization spectrum — the polarization fraction as a function of wavelength — and find that it depends more strongly on column density than dust temperature. We find a “falling” spectrum at the 0.052 pc resolution, but find a “flat” spectrum at the 0.32 pc resolution, suggesting that resolution plays an important role in the observed polarization spectra. We propose that warm dust grain emission in small-scale structures ($\lesssim 0.1$ pc) traces different magnetic field geometries only resolved in our close regime data. There is no preferred magnetic field orientation across our data, which suggests that the magnetic field in our \sim parsec scale regions is decoupled from the large-scale field that is primarily parallel to the Galactic plane. The relationship between percent polarization and column density varies between clouds, but the correlation between percent polarization and angular dispersion is consistent across regions. This compendium of dust polarization maps highlights the value of observing at multiple far-infrared wavelengths and will enable additional population-level studies of magnetic fields and dust across star-forming environments.

Keywords: Interstellar magnetic fields (845) - Polarimetry (1278) - Far infrared astronomy (529) - Molecular clouds (1072)

1. INTRODUCTION

Star formation typically occurs in the densest parts of molecular clouds; however, it has been known for decades that star formation occurs at a rate lower than expected from the masses of molecular clouds (e.g., Zuckerman & Evans 1974; Krumholz & Tan 2007). Proposed explanations for this often invoke magnetic fields and/or turbulence to explain the low rate of star formation (e.g., Mouschovias & Spitzer 1976; Mac Low & Klessen 2004; Federrath & Klessen 2012). Understanding the interplay between magnetic fields, turbulence, and gravity is crucial for understanding the complete picture of star formation efficiency.

Methods to observe the plane-of-sky magnetic field orientation in molecular clouds include optical/near-infrared absorption polarization (Davis & Greenstein 1951) and far-infrared/submillimeter emission polarization (Hildebrand et al. 2000). Far-infrared wavelengths, typically defined as $\lambda \sim 50 - 300 \mu\text{m}$, are ideal for studying magnetic fields through polarized dust emission, because thermal dust emission peaks in the far-infrared, where both warm ($\sim 30 - 60$ K) and cold ($\sim 10 - 30$ K) dust populations contribute significantly to the observed flux. Plane-of-sky magnetic fields

can be observed via the polarized radiation from elongated dust grains that align their short axes with the magnetic field. The leading explanation for how grains become aligned involves Radiative Alignment Torques (RAT), in which paramagnetic grains rotate suprathermally and induce a magnetic moment due to the Barnett Effect Dolginov & Mitrofanov 1976; Draine & Weingartner 1997; Lazarian & Hoang 2007.

Multiwavelength observations of polarized dust emission are particularly valuable. Dust polarization spectra in the far-infrared and submillimeter, which quantify how the percent polarization changes as a function of wavelength, are important for understanding the physical properties of interstellar dust grains (e.g., Draine & Hensley 2021) and grain alignment (e.g., Bethell et al. 2007; Lee et al. 2024; Tram, Le Ngoc et al. 2024). The submillimeter spectra have been observed to be relatively flat (e.g., Ashton et al. 2018; Hensley & Draine 2021). However, some observations have found that the far-infrared portion of the spectrum in molecular clouds can have a “V” shape, with the polarization fraction decreasing with wavelength (falling) until about 300 μm , and then increasing (rising) at longer wavelengths (Vailancourt 2002). This complex spectral dependence can be

caused by having multiple cloud components with different temperatures along the line of sight. Studying the polarization spectrum as a function of cloud properties such as temperature and density can be used to understand the three-dimensional geometry of clouds (Lee et al. 2024; Seifried et al. 2025).

There have been studies in the far-infrared wavelength range that explore the polarization properties in molecular clouds using instruments on the Kuiper Airborne Observatory (KAO) and the Caltech Submillimeter Observatory (CSO) (e.g., Hildebrand et al. 1999; Vaillancourt 2002; Stephens et al. 2011). The Planck satellite has also been used to study polarized Galactic emission at 353 GHz ($\sim 850 \mu\text{m}$), revealing the large-scale structure of magnetic fields in the diffuse and moderately dense interstellar medium (e.g., Planck Collaboration et al. 2020a, 2015a). However, Planck’s angular resolution is $4.94'$ at 353 GHz and to get high enough signal to noise the data are often smoothed to a resolution of $10'$ or worse (e.g., Planck Collaboration et al. 2020a, 2016).

The most recent far-infrared polarimeter was the High-resolution Airborne Wideband Camera-Plus (HAWC+; Harper et al. 2018) on the Stratospheric Observatory For Infrared Astronomy (SOFIA). HAWC+ observed linear polarization in the far-infrared at wavelengths of 53, 89, 154, and $214 \mu\text{m}$. The resolution of the HAWC+ data ($\leq 18.2''$) allows the study of sub-parsec structure in molecular clouds out to a distance of ~ 10 kpc. Compared to instruments like Planck, HAWC+ is able to resolve higher-density structures, with our work finding column densities in the range $N_{H_2} \sim 10^{22} - 10^{23} \text{ cm}^{-2}$. These dense regions may contain substantial substructure, including $\lesssim 0.1$ pc hot molecular cores with temperatures ~ 100 K (Cesaroni 2005; André et al. 2010); filaments with widths of order ~ 0.1 pc (Arzoumanian et al. 2011; Hennemann, M. et al. 2012; Schisano et al. 2014); and denser sub-filaments (Fernández-López et al. 2014; Hacar et al. 2013).

Currently, there are no studies using a large compilation of HAWC+ datasets over a wide variety of molecular clouds. Many works are comprehensive studies of the properties of a single cloud at a time (e.g., Santos et al. 2019; Chuss et al. 2019; Zielinski & Wolf 2022; Pillai et al. 2020; Bij et al. 2024; Hoang et al. 2022; Sarkar et al. 2025; Seo et al. 2021) or multiple components of one cloud complex (e.g., Lee et al. 2021; Barnes et al. 2025). There are some works that look at multiple diverse clouds like the three clouds studied in Cox et al. (2025) and the ten “bones” studied in Stephens et al. (2025) and Coudé et al. (2025). However, the full potential of archival HAWC+ observations of molecular clouds has yet to be realized.

To understand the properties of magnetic fields and polarization broadly across diverse environments, we compile a large sample of 52 archival SOFIA/HAWC+ datasets, over half of which are currently unpublished. Our data include 26 star-forming regions spanning distances from 130 to 2620 pc. We also use data at wavelengths of 70, 100, 160, 250, and $350 \mu\text{m}$ from the Herschel Space Observatory to derive

temperature and column density maps. We analyze the data at common angular and common physical resolutions to determine the effects of resolution and distance on polarization properties. We choose two physical resolutions of 0.052 pc and 0.32 pc, with the smaller scale able to resolve many small cores and filaments.

This paper is organized as follows: we first describe the far-infrared data products and processing from the HAWC+ instrument on SOFIA and the Herschel Space Observatory (Section 2); we discuss our selected compilation and detail how we separate them into regimes by distance (Section 3); we describe how we compute the derived quantities of column density, temperature, and angular dispersion we need for our analyses (Section 4); and we detail our analyses and results in the context of past literature (Section 5). Finally, we present a summary of our key results in Section 6.

2. OBSERVATIONS

2.1. HAWC+ Data

We use 52 archival imaging polarimetric datasets from the HAWC+ (Harper et al. 2018) instrument on SOFIA. HAWC+ observed in four wavelength bands centered on $53 \mu\text{m}$ (bandwidth $\Delta\lambda = 8.7 \mu\text{m}$, Band A), $89 \mu\text{m}$ ($\Delta\lambda = 17 \mu\text{m}$, Band C), $154 \mu\text{m}$ ($\Delta\lambda = 34 \mu\text{m}$, Band D), $214 \mu\text{m}$ ($\Delta\lambda = 44 \mu\text{m}$, Band E) with resolutions of $4.85''$, $7.8''$, $13.6''$, and $18.2''$, respectively. Our collection consists of nine Band A, twelve Band C, fifteen Band D, and sixteen Band E maps, and we note the available bands for each region in Table 1. We have only chosen datasets that were observed using the chop-nod mode of HAWC+ because the on-the-fly mapping (OTFMAP) mode requires a different reduction algorithm (Lopez-Rodriguez et al. 2022). The on-the-fly mapping mode also does not effectively recover large-scale features in the data (Lopez-Rodriguez et al. 2022), which we need for our analyses at common angular and physical resolutions.

Data were reduced using the SOFIA Redux pipeline¹. Some of the data on the archive needed to be re-reduced, either because the only level 4 products available were produced with an outdated version of the pipeline or because the level 4 products did not include all of the available observations for the region. The final data used are a combination of level 4 data downloaded from the SOFIA/HAWC+ archive that used version 3.2.0 of the pipeline, data we reduced using version 2.7.0 of the pipeline, and data reduced for Chuss et al. (2019) using version 1.3.0beta3 of the pipeline. There were no substantial differences in the chop-nod data reduction between versions 3.2.0 and 2.7.0. The updates between these versions focused mainly on the data reduction for the OTFMAP observations and minor bug fixes¹. We confirm that the versions produce similar results by re-reducing data with version 2.7.0 and comparing the results with data on the archive reduced with version 3.2.0. Even though Chuss et al. (2019) used an older version of the pipeline, we still

¹ <https://irsa.ipac.caltech.edu/data/SOFIA/docs/data/data-pipelines/>

use their data because their reduction and processing takes into account potential background contamination from off-axis chops. Table A.1 denotes which pipeline was used for each dataset. We reduce the data with the default parameters and remove files that were flagged by the archive quality assurance notes for data quality issues. We also check the individual files produced by the ‘‘Calibrate Flux’’ step in the pipeline to look for and remove anomalies that impact the final merged maps. The headers of the final FITS files denote the raw files used.

Bands A and C from the W3 region included data observed in the ‘‘Standard Flux’’ mode in addition to the usual mode. To reduce these data into a single map, we force the pipeline to reduce all the data in NODPOL mode instead of NODPOL_STD by replacing the steps used in the pipeline for the NODPOL_STD mode with the step of the NODPOL mode.

The final data products are maps of the linear Stokes parameters (I , Q , and U) from which maps of the percent polarization (p) and the polarization angle (ϕ) are computed, along with statistical uncertainties.

$$p = \frac{\sqrt{Q^2 + U^2}}{I} \quad (1)$$

$$\phi = \frac{1}{2} \arctan2(U, Q) \quad (2)$$

The uncertainties on p (σ_p) and ϕ (σ_ϕ) are propagated as

$$\sigma_p = \frac{1}{I} \sqrt{\frac{(\sigma_Q Q)^2 + (\sigma_U U^2)}{Q^2 + U^2} + \frac{\sigma_I^2}{I^2} (Q^2 + U^2)} \quad (3)$$

$$\sigma_\phi = \frac{1}{2} \frac{1}{Q^2 + U^2} \sqrt{(\sigma_U Q)^2 + (\sigma_Q U)^2}. \quad (4)$$

Our polarization orientation is defined in the IAU convention, where positive ϕ is measured counterclockwise from North when looking toward the source. Due to its strictly positive nature, p is strongly biased at low signal-to-noise (Plaszczynski et al. 2014). We debias p using its statistical uncertainty as follows:

$$p_{debiased} = \sqrt{p^2 - \sigma_p^2}. \quad (5)$$

We use $p_{debiased}$ for all of our analyses and will hereafter refer to it as p . We then apply signal-to-noise cuts to only include data that satisfy $I/\sigma_I \geq 200$ and $p/\sigma_p \geq 3$.

2.2. Herschel data

We also use archival total intensity data from the Photodetector Array Camera and Spectrometer (PACS; Poglitsch

et al. 2010) and Spectral and Photometric Imaging REceiver (SPIRE; Griffin et al. 2010) instruments on the Herschel Space Telescope to fit modified blackbody functions in each region. PACS observed at 70 μm , 100 μm , and 160 μm . The angular resolution at each wavelength is lengthened along the scan direction with a magnitude of elongation that depends on the scan speed and whether the observation was taken in the PACS/SPIRE parallel mode, which is modeled as a two-dimensional Gaussian as described in Poglitsch et al. (2010). When smoothing the PACS data, we use the geometric mean of the two Gaussian widths for each dimension as the native resolution of the data. For the 70 μm and 160 μm data, we have a combination of data sets taken at 20 arcsec/sec and 60 arcsec/sec in parallel mode. All of the 100 μm data were observed at 20 arcsec/sec. This results in native resolutions of 5.6'' and 8.4'' (70 μm), 6.8'' (100 μm), and 11.2'' and 13.4'' (160 μm). We also use 250 μm and 350 μm SPIRE data, which have angular resolutions of 18.2'' and 25''. We smooth to the resolution of the SPIRE 350 μm data as they are the lowest resolution data between both Herschel and HAWC+. We adopt uncertainties of 20% for PACS and 10% for SPIRE (Poglitsch et al. 2010; Griffin et al. 2010). Not every region had observations at all five wavelengths and we note which wavelengths were used in Table 1.

The thermal dust spectral energy distribution (SED) is not constant across the wide Herschel filters, and is instead characterized by a slope that depends on the source’s spectral index and temperature. We thus apply color correction factors to both the PACS and SPIRE data. The color corrections are tabulated in Müller et al. (2011) and the SPIRE handbook² as a function of blackbody temperature and spectral index. Preliminary fits of the intensity data without color corrections showed a general temperature range between 15 K and 60 K and a spectral index range between 1 and 2. To determine the color correction factors, we average the values in the tables of Müller et al. (2011) and the SPIRE handbook for this range of temperatures and spectral indices. This results in multiplicative correction values of 0.843, 0.996, 0.986, 0.991, and 0.981 for the 70 μm , 100 μm , 160 μm , 250 μm , and 350 μm bands, respectively. After applying these color correction factors, the resulting temperatures and spectral indices still fall within the original ranges.

Region	RA (°)	Dec (°)	HAWC+ Bands	Herschel λ (μm)	Distance (pc)	Distance Reference	β
L1527	69.978	26.046	D	70, 160, 250, 350	130	Roccatagliata et al. (2020)	1.00 ± 0.01
L1688	246.628	-24.394	A, C, D	70, 100, 160, 250, 350	139	Zucker et al. (2020)	1.50 ± 0.02

² http://herchel.esac.esa.int/Docs/SPIRE/spire_handbook.pdf

ρ Oph E/F	246.782	-24.626	D	70, 100,160, 250, 350	139	Zucker et al. (2020)	1.00±0.001
L1689N	248.094	-24.476	C, D	100,160, 250, 350	147	Ortiz-León et al. (2017)	1.10±0.04
NGC 1333	52.291	31.369	C, E	70, 100,160, 250, 350	299	Zucker et al. (2018)	1.00±0.001
OMC1	83.803	-5.371	A, C, D, E	70, 100,160, 250, 350	388	Kounkel et al. (2017)	2.02±0.01
OMC2/3	83.809	-4.983	D, E	70, 100,160, 250, 350	388	Kounkel et al. (2017)	1.43±0.01
NGC 2071	86.768	0.361	E	70, 100,160, 250, 350	388	Fedriani et al. (2022)	1.00±0.004
NGC 2068	86.651	0.042	E	70, 100,160, 250, 350	388	Kounkel et al. (2017)	1.64±0.01
Serpens	277.506	-2.054	E	70, 100,160, 250, 350	432	Ortiz-León et al. (2018)	1.00±0.0002
Vela C	134.839	-43.767	C, E	70, 160, 250, 350	933	Fissel et al. (2019)	1.66±0.01
S106	306.855	37.388	A, E	70, 160, 250, 350	1091	Zucker et al. (2020)	1.68±0.01
NGC 6334	260.078	-35.914	A, C, D, E	70, 160, 250, 350	1350	Wu et al. (2014)	1.96±0.01
DR21	309.754	42.378	A, E	70, 160, 250, 350	1400	Rygl et al. (2012)	1.81±0.02
G34.43	283.340	1.421	E	70, 160, 250, 350	1560	Kurayama et al. (2011)	1.24±0.02
M17	275.097	-16.211	A, C, D, E	70, 100,160, 250, 350	1600	Zucker et al. (2020)	1.54±0.01
G14.2N	274.551	-16.837	D	70, 160, 250, 350	1600	Díaz-Márquez et al. (2023)	1.18±0.02
G14.2S	274.551	-16.957	D	70, 160, 250, 350	1600	Díaz-Márquez et al. (2023)	1.24±0.02
M16	274.719	-13.833	C, D	70, 160, 250, 350	1700	Zucker et al. (2020)	1.60±0.02
G351.77	261.662	-36.121	E	70, 160, 250, 350	2000	Reyes-Reyes et al. (2024)	1.24±0.01
W3OH	36.764	61.874	A, C, D, E	70, 160, 250, 350	2000	Navarete et al. (2019)	1.18±0.01
W3	36.417	62.104	A, C, D, E	70, 160, 250, 350	2300	Navarete et al. (2019)	1.95±0.01
W33	273.558	-17.928	A, C, E	70, 160, 250, 350	2400	Immer et al. (2013)	1.83±0.02
BYF77	159.437	-58.772	D	70, 160, 250, 350	2500	Vazzano et al. (2014)	1.74±0.01
BYF73	159.634	-58.311	D	70, 160, 250, 350	2500	Barnes et al. (2010)	1.41±0.02
Keyhole	161.220	-59.654	C	70, 160, 250, 350	2620	Kuhn et al. (2019)	1.43±0.01

Table 1. A table of every region included in our compilation, with their location in equatorial coordinates, the available Herschel wavelengths, their distances and reference, and the dust emissivity index determined in Section 4. Every region above the single solid line is in the close regime (130-432 pc) and every region below the double solid line is in the far regime (299-2620 pc).

3. COMPILATION

Our 52 dataset compilation comprises of data from 26 nearby star-forming regions from the SOFIA/HAWC+ archive that were observed with the chop-nod method and resulted in significant polarization detections. Our data cover a range of objects such as molecular clouds, filamentary clouds, infrared dark clouds (IRDCs), prestellar cores, and protostellar cores. HAWC+ observations cover some of the highest H_2 column density portions of the clouds ($\sim 10^{22} - 10^{23} \text{ cm}^{-2}$). While we may not directly measure emission from HII regions, young stellar objects (YSOs), and MASERS within these larger objects, they often dictate the observation centers and target names. Figure 1 shows the location of every region in our compilation overlaid on an all-sky map of the Planck 857 GHz emission data (Planck Collaboration et al. 2020b). In Table 1, we list every region used in this analysis with its equatorial coordinates and a literature estimate of its distance from the Sun. We include a citation for every distance we use in the sixth column. In Figure 2 we show an example map from each region using the band with approximately largest spatial coverage. While we do not have uniform wavelength coverage for every re-

gion, Figure 3 shows our regions that do have observations in all four HAWC+ bands. The rest of our HAWC+ data not included in Figure 2 or Figure 3 are shown in Figure A.1.

For some of our analysis we smooth subsets of our data to a common physical resolution. We smooth the data by convolving with a Gaussian kernel. The map is then rebinned so that the width of four pixels equals the final beam full width at half maximum ($FWHM$) (i.e., Nyquist sampling). We propagate the uncertainties on the linear Stokes parameters by dividing the unsmoothed uncertainty at each pixel by \sqrt{n} where $n = FWHM_f^2 / FWHM_i^2$, the ratio of the final to the initial $FWHM$. The farthest region in a given distance bin determines how coarsely we must smooth the nearest regions. To ensure we have enough independent measurements (> 3) in each region after smoothing to a common physical resolution in the nearest regions, we define two subsets of data: a close regime ($D < 432$ pc) and a far regime ($299 < D < 2620$ pc). Both regimes include the regions with distances $299 < D < 432$, because these regions have more than 3 independent measurements when smoothed to the constant physical resolution of the far regime. The minimum number of independent measurements in a region in

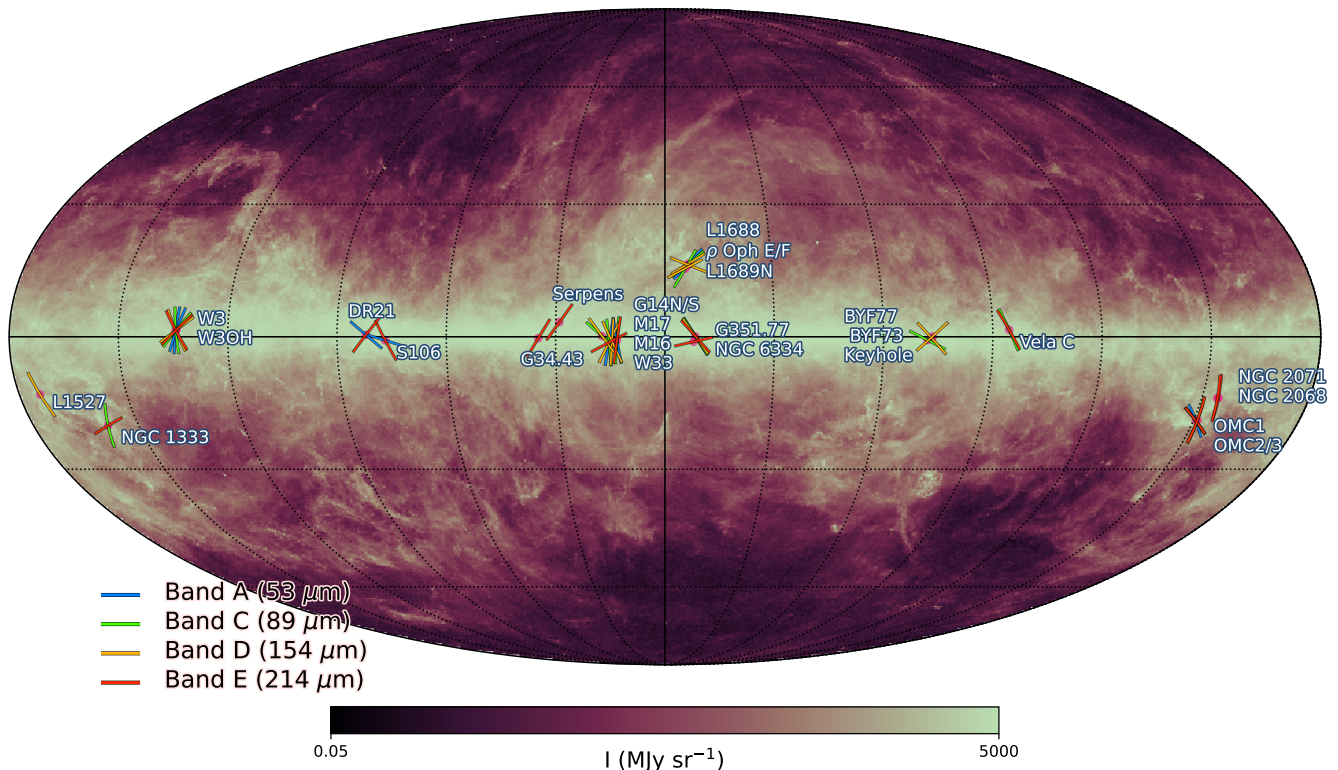


Figure 1. Sky distribution of the 26 regions used in this paper. Each region is marked with a pink dot on a galactic projection full-sky map of the Planck 857 GHz data with histogram equalized color mapping. The vectors represent the average magnetic field orientation for each region as a function of wavelength (colors shown in legend).

both regimes is 3, but most regions greatly exceed our minimum threshold. There are 10 regions in the close regime and 22 regions in the far regime, with 6 regions included in both regimes.

The data are smoothed to the physical resolution of the Herschel 350 μm data resolution ($25''$) at 432 pc and 2620 pc, which results in resolutions of 0.052 pc and 0.32 pc, respectively. For our analyses, it is important to note that multiple regions in the close regime are near the 432 pc distance cut, meaning they are not smoothed with a large kernel in the common physical resolution analyses. Because of this, we do not necessarily expect large changes when we smooth the close regime data. We also note that one of the regions in the overlap is OMC1, which can contribute a large number of data points in all four bands at the common angular resolution due its large spatial coverage. The trends we see in our compilation remain when we remove OMC1, so we do not believe OMC1 is significantly biasing our results.

4. DERIVED PROPERTIES

In addition to the observed polarization properties, we utilize three derived quantities: the column density, temperature, and polarization angular dispersion. We fit a modified blackbody curve to the Herschel data described in Section 2.2 to estimate the column density, dust temperature, and dust emissivity index. The fit is performed in each region three separate times on Herschel data that is smoothed to the com-

mon angular resolution ($25''$) and the common physical resolutions (0.052 pc and 0.32 pc). We follow the method for modified blackbody curve fitting described in Chuss et al. (2019).

The intensity is modeled as:

$$I_\nu = (1 - e^{-\tau(\nu)})B_\nu(T), \quad (6)$$

where $B_\nu(T)$ is the Planck blackbody function at frequency (ν) and temperature (T). The optical depth, $\tau(\nu)$, is defined as $\tau \equiv \epsilon(\frac{\nu}{\nu_0})^\beta$, where ϵ is a constant of proportionality related to the column density along the line of sight and β is the dust emissivity index. We use a value of 1000 GHz for ν_0 and $\epsilon = \kappa_{\nu_0} \mu m_H N_{H_2}$. κ_{ν_0} is a reference dust opacity per unit mass at ν_0 , μ is the mean molecular weight per hydrogen atom, m_H is the atomic mass of hydrogen, and $N(H_2)$ is the gas column density. We use $\kappa_{\nu_0} = 0.1 \text{ cm}^2 \text{ g}^{-1}$ and $\mu = 2.8$ following Sadavoy et al. (2013).

In star-forming regions, β can vary generally between ~ 1 and 3 (e.g., Hunter 1998; Friesen et al. 2005; Chuss et al. 2019). These variations can be caused by different dust grain compositions or from fitting a single temperature to a system with multiple temperature components along the line of sight (Draine 2006). Because of this, we do not wish to choose a single constant value of β to apply to every sightline in every region. However, there is a fitting degeneracy between β and T that makes it hard to fit a modified blackbody, especially for higher temperature objects, with only four or five

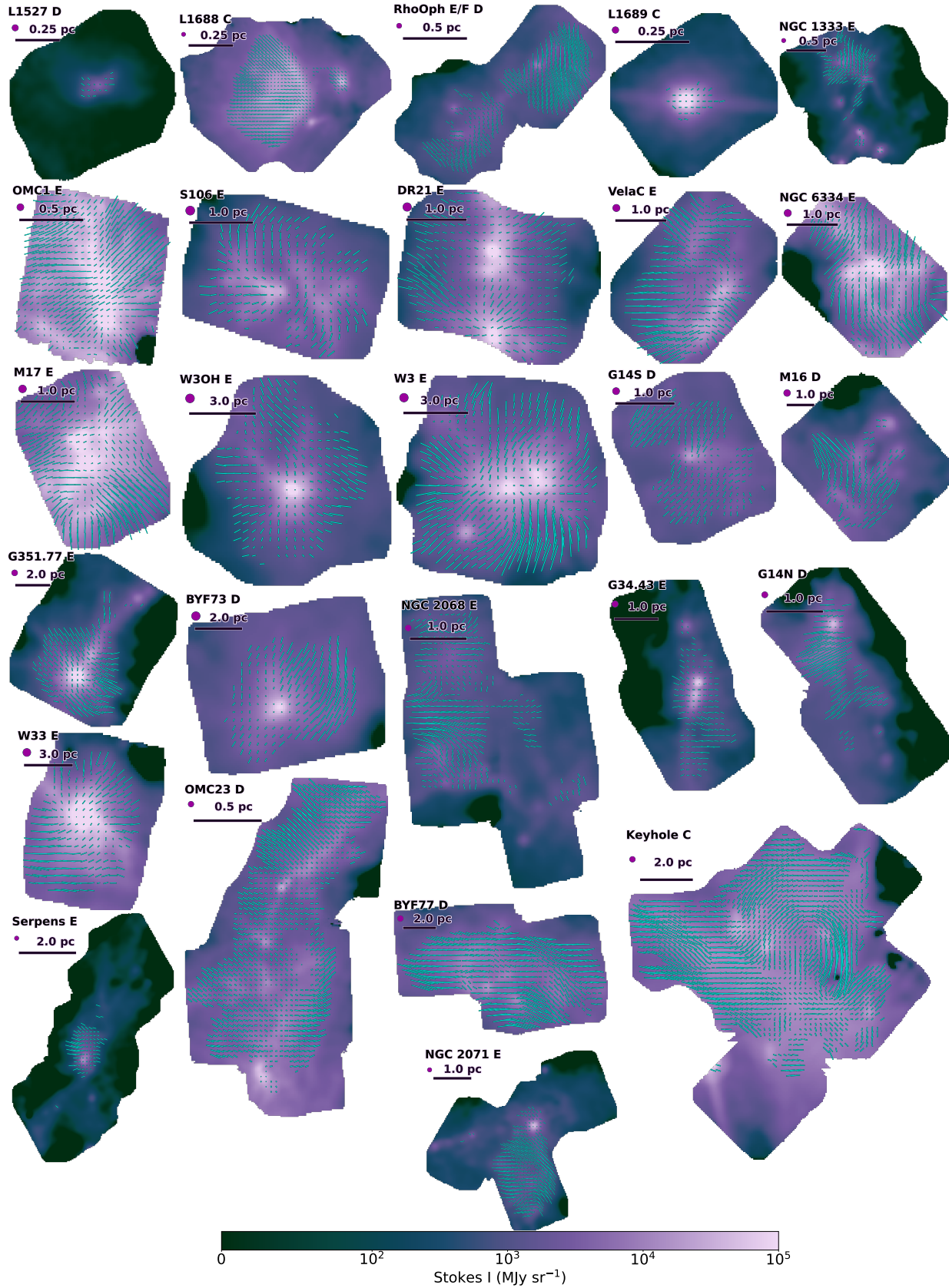


Figure 2. A representative HAWC+ dataset from each of the 26 regions. Each region is labeled with its name and a letter denoting the HAWC+ band shown. The purple circle shows the beam size. The vectors are the magnetic field pseudovectors and their length corresponds to the percent polarization. The pseudovectors are sampled so there is one vector per beam. The scale bar denotes the physical size in parsecs calculated from the distances in Table 1.

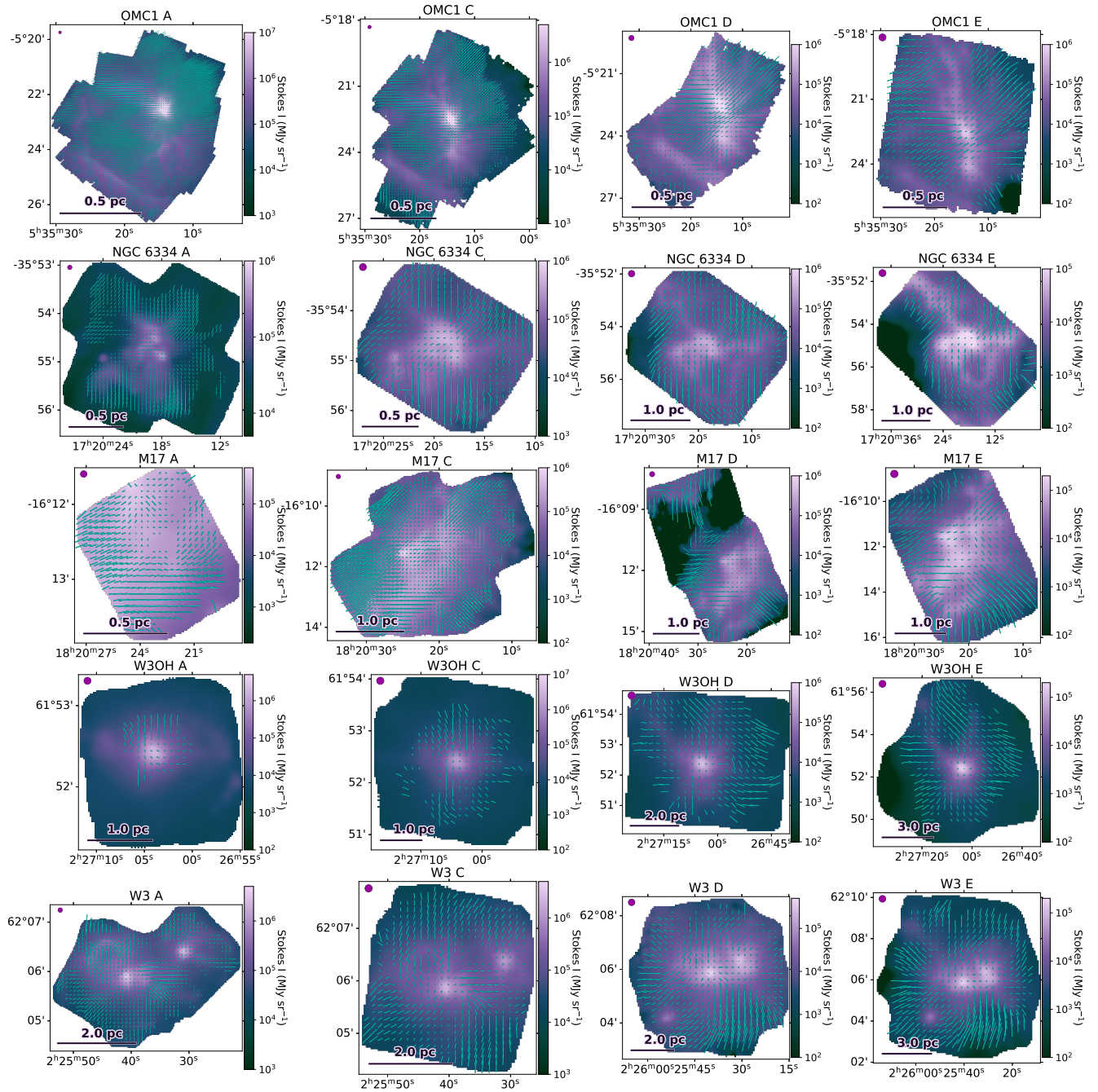


Figure 3. Same as Figure 2 for the regions that we have coverage in all four HAWC+ bands.

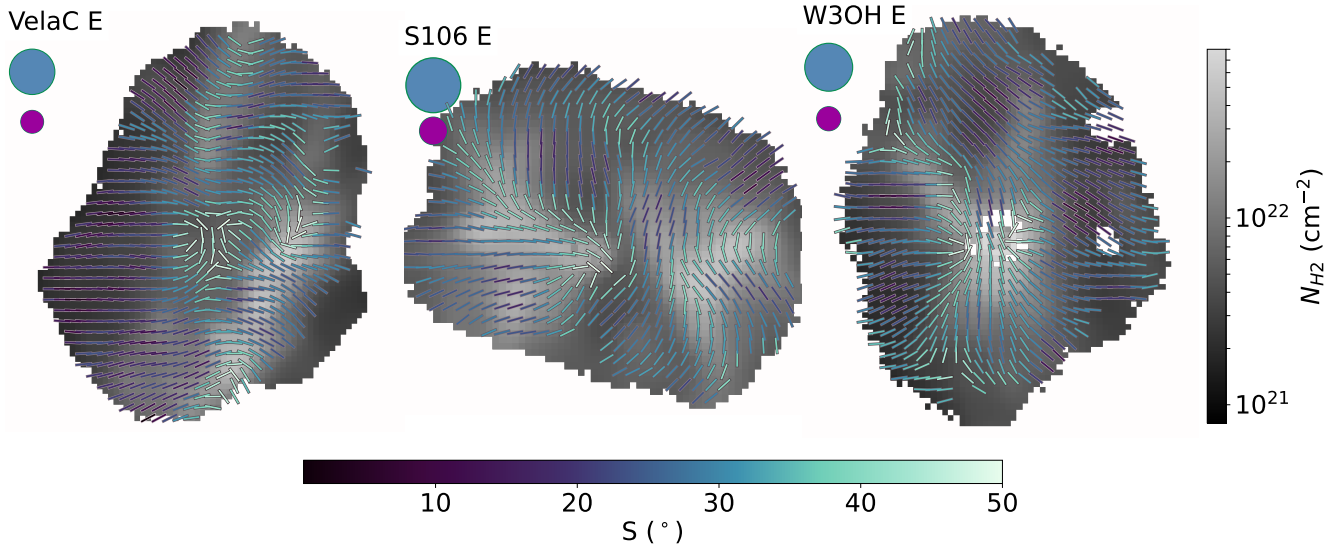


Figure 4. Example maps of the column density with magnetic field pseudovectors overlaid. The vectors are color coded by the angular dispersion and have constant length. The blue circle shows the size of the disk that the dispersion is calculated over and the purple circle shows the $25''$ beam.

data points for each pixel (Shetty et al. 2009). We decide to fit for a different β value for each region that is then used for every pixel in that region. To do this, we create a footprint from the HAWC+ data that satisfy $I/\sigma_I \geq 200$ for any wavelength for a region, and use this as a mask on the Herschel data. The pixels within this mask are then used to find a single β value that produces the lowest χ^2 map when used in fitting a map of temperature and column density. For some regions, the fit preferred values of β that were below 1, which has been observed in protoplanetary disks likely due to dust grain growth, but is not expected for dust in molecular clouds (Draine 2006). Our data are not sensitive to individual protoplanetary disks, which have radii of 10s to 100s of au (Trapman et al. 2023), so we do not physically expect β to be less than 1. We use a flat prior on $\beta > 1$, but to discourage fitting $\beta < 1$, we use a prior equal to β^2 for $\beta < 1$. A Markov-Chain Monte Carlo (MCMC) method is used to estimate the uncertainty on β . These values are reported in Table 1. We then use this constant β value and the Herschel intensity maps to fit for maps of the temperature and column density, using a MCMC method to determine their uncertainties. We use the β value derived from the $25''$ for the 0.052 pc and 0.32 pc fits. After completing the fits, we calculate the reduced χ^2 statistic for each pixel. For our analyses, we only use pixels where $\chi_{reduced}^2 < 3$. Figure 4 shows three example plots of our derived column density maps that satisfy the $\chi_{reduced}^2 < 3$ cut at a resolution of $25''$ with magnetic field pseudovectors overlaid. For some of the Herschel datasets, there are saturation effects at the brightest peaks, resulting in worse fits to the modified blackbody spectrum, resulting in those pixels being cut from our analyses. This can be seen in the derived column density map shown in W30H in Figure 4, where some of the center pixels were cut.

The per-pixel angular dispersion (S) is calculated from the HAWC+ maps as the circular standard deviation of all pixels within a disk around each map pixel. The circular standard deviation for polarization pseudovectors is defined as

$$S = \frac{1}{2} \sqrt{-2 \ln(\bar{R})}, \quad (7)$$

where \bar{R} is the resultant length and can be defined as

$$\bar{R} = \frac{1}{N} \sqrt{\left(\sum \sin 2\phi\right)^2 + \left(\sum \cos 2\phi\right)^2}. \quad (8)$$

We calculate S using the linear Stokes parameters where $\sin 2\phi = \frac{U}{\sqrt{Q^2+U^2}}$ and $\cos 2\phi = \frac{Q}{\sqrt{Q^2+U^2}}$.

The uncertainty on S is estimated using a Monte Carlo method, by randomly sampling within the uncertainties on Stokes Q and U . S always has a positive value and is biased by noise. S is debiased using its uncertainty

$$S_{debiased} = \sqrt{S^2 - \sigma_S^2}, \quad (9)$$

but σ_S is generally a small quantity (fractions of a degree), so we note that debiasing does not have a noticeable impact on the results in this paper. We use $S_{debiased}$ for all of our analyses and will hereafter refer to it as S . We calculate S using radii of 1, $\frac{3}{2}$, and 2 beams. We show the distributions of S in all the data, the close regime, and far regime, for each of these radii in Figure 5. Further analysis in Section 5.5 is done using S calculated over a disk of radius of 1 beam. We also calculate S for the smoothed data, where the dispersion is calculated over a constant physical scale that has a diameter of two beams. The pseudovectors in Figure 4 are colored by the value of S calculated over a disk of radius 1 beam ($25''$).

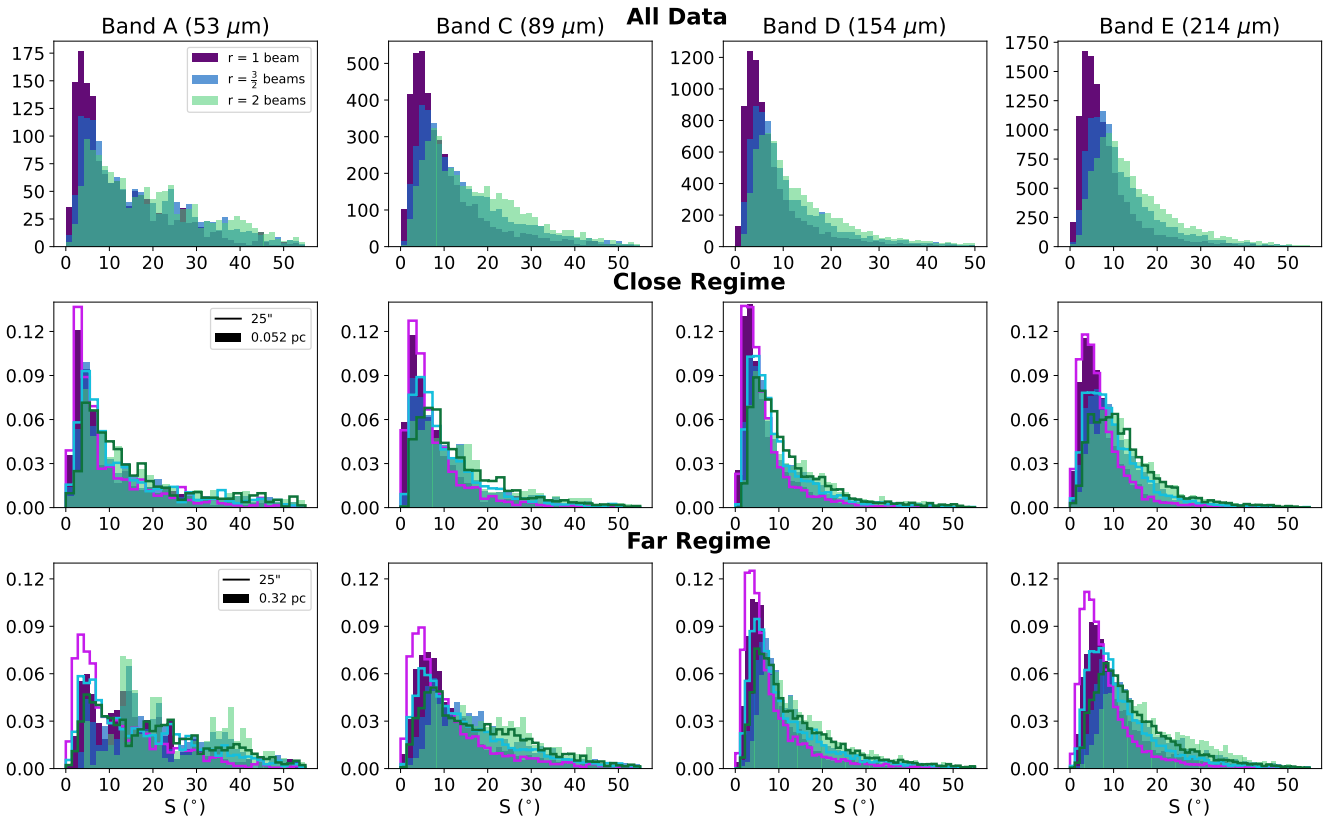


Figure 5. Histograms of the angular dispersion calculated over three different areas with radii of 1, 3/2, and 2 beams. *Top:* All of the data smoothed to 25". *Middle:* The close regime data smoothed to 25" (solid lines) and smoothed to 0.052 pc (shaded regions). *Bottom:* The far regime data smoothed to 25" (solid lines) and smoothed to 0.32 pc (shaded regions).

5. RESULTS AND DISCUSSION

5.1. Percent Polarization

With a large population of star-forming regions at various distances and locations in the galaxy, we search for common trends in the plane-of-sky polarization data. We start by investigating the distributions of p in all HAWC+ bands (53–214 μm) at both common angular and physical resolutions, shown in Figure 6. We report the median, first quartile, and third quartile values on each plot. In the top row, we show a stacked histogram where the data are colored based on the distance of the region they come from. In Bands A and C, we see a generally negative trend between p and distance, where the largest p are in the closest regions. The maximum p detected in each band is $\sim 15 - 20\%$. The highest p values (around $\sim 20\%$) are in the Bands D and E data.

A similar analysis with a sample of 14 star-forming regions was done at wavelengths of 60 μm and 100 μm from the STOKES polarimeter on the Kuiper Airborne Observatory (KAO) and at 350 μm from the Hertz polarimeter on the Caltech Submillimeter Observatory (CSO; Hildebrand et al. 1999). The resolutions of these observations were 22" (Dowell 1997), 35" (Platt et al. 1991), and 20" (Dowell et al. 1998) for 60 μm , 100 μm , and 350 μm respectively. This work included multiple nearby regions that we also use in our analysis, but their data also extended to larger distances, includ-

ing multiple clouds in the Galactic Center. Hildebrand et al. (1999) observed a distribution of p that was generally in the range $0\% \lesssim p \lesssim 10\%$. They also saw the broadest distribution of p at their shortest wavelength of 60 μm .

Compared to this previous work, we find a larger range in p , as significant portions of our data have values above 10%. Bands A and C in the close regime have the broadest distributions, as quantified by the interquartile range (Figure 6). The far regime also shows a larger interquartile range in Bands A and C in the common angular resolution data, but it is less pronounced than in the close regime. If the polarization efficiency of the grains varies as a function of the grain temperature, we would expect the distributions of p to vary between the bands, as the shorter wavelengths are more sensitive to warmer dust grains. p can also vary between bands if these data probe distinct grain populations with different degrees of magnetic field tangling, as a more tangled field will result in more depolarization and lower p .

We also analyze how the resolution of data impacts the distributions of p . The distributions of p in the close regime do not change greatly when smoothed to a common physical resolution (0.052 pc). This is likely because multiple regions in the close regime do not need to be smoothed with large kernels to get to the final resolution. The distributions of p in the far regime change more when smoothed to a common

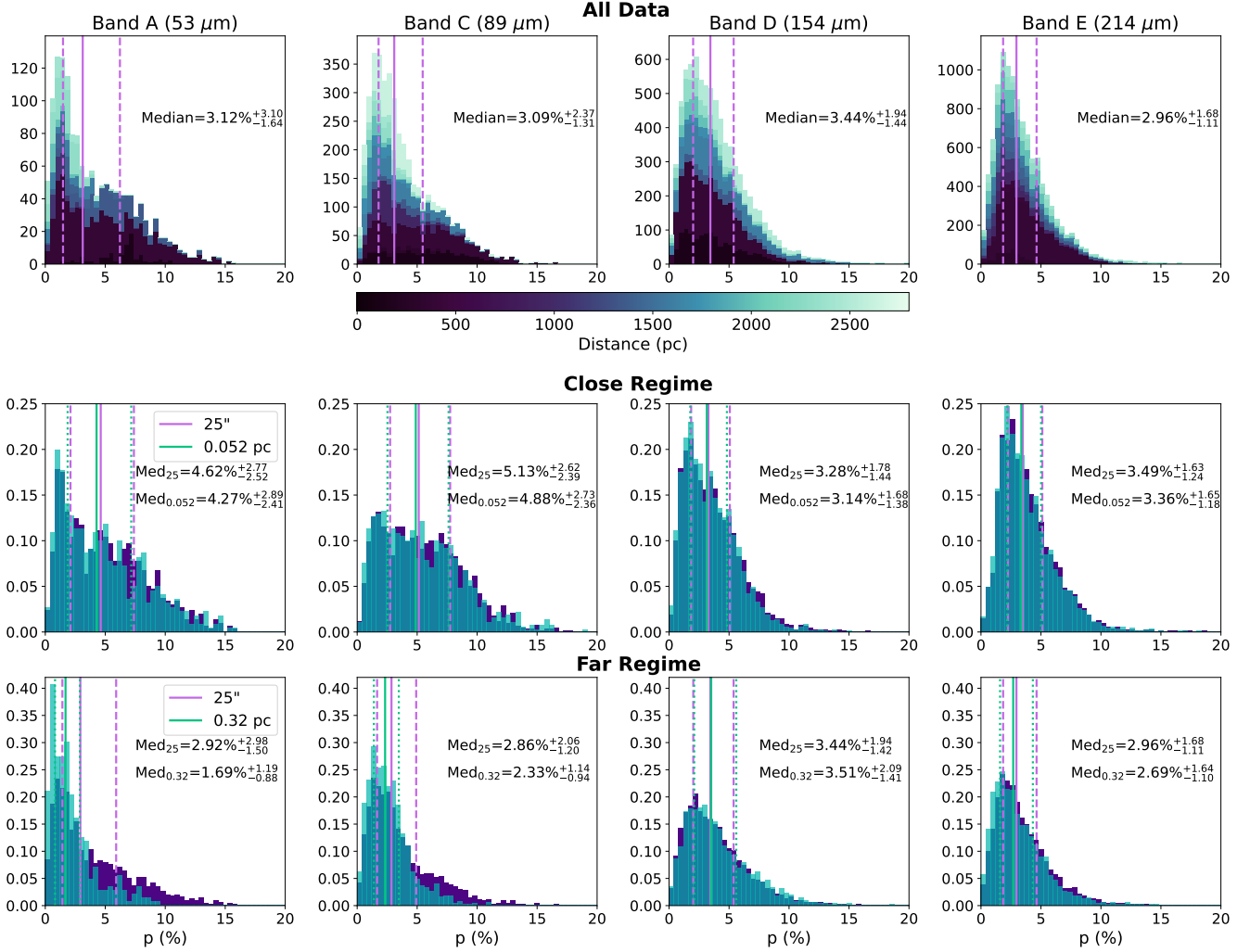


Figure 6. Histograms of the percent polarization. *Top:* All of the data in a stacked histogram smoothed to $25''$. The data are colored based on their distance. *Middle:* Density histograms of the data in the close regime smoothed to $25''$ (purple) and smoothed to 0.052 parsec (cyan). *Bottom:* Density histograms of the data in the close regime smoothed to $25''$ (purple) and smoothed to 0.32 parsec (cyan). The medians with first and third quartiles are denoted in text on the plots. The solid line is the median value and the two segmented lines show the first and third quartiles.

physical resolution (0.32 pc). The most dramatic change is a decrease in the high- p tail of the distributions in Bands A and C. We analyzed the distributions of p in each region individually at the common angular resolution. We find that the more nearby regions (smallest physical resolution initially) generally had the highest p at $25''$ resolution in Bands A and C, and then once smoothed to the same physical resolution for the far regime, all the regions had similar p distributions to the farthest dataset. Conversely, the p distribution in Bands D and E in the far regime show no significant change when smoothed to a common physical resolution and also do not show a dependence on distance before smoothing.

Smoothing the data will generally lower the percent polarization if the new beam size averages over regions of high and low p or varied polarization orientation (beam depolarization). We can see in Figure 5 that the high S tails in Bands

A and C are larger, signifying that there is more variation in the polarization angle orientations. This is consistent with the observation that smoothing to a common physical resolution disproportionately affects the shorter wavelengths. Star-forming regions exhibit structure on many scales, from filaments that are generally observed to have widths on the order of ~ 0.1 pc (Arzoumanian et al. 2011; Hennemann, M. et al. 2012; Schisano et al. 2014; Fernández-López et al. 2014; Panopoulou et al. 2022) to dense cores that often have sizes in the range $\sim 0.01 - 0.1$ pc (Cesaroni 2005; André et al. 2010). The observed polarization structure of our shorter-wavelength bands could be caused by pockets of warmer dust within our regions, if these are associated with small-scale magnetic field structure. In the temperature maps of some of our regions, we do see evidence of small warmer cores with temperatures ~ 50 K. The scale dependence of the po-

larized dust emission could be further probed by measuring polarization power spectra of these regions (e.g., Planck Collaboration et al. 2020c; Córdova Rosado et al. 2024). Such analyses would be better enabled by high sensitivity observations with larger dynamic range, e.g., as could be achieved with the proposed PRobe Infrared Mission for Astrophysics (PRIMA; Glenn et al. 2025).

5.2. Polarization Spectra

We use our compilation to broadly understand polarization spectra — the change in p with wavelength — in Galactic molecular clouds. Using the median values of the p distributions in Figure 6, we observe diverse behaviors across our regimes. In the close regime, p is generally higher in Bands A and C, approximating a falling polarization spectrum (decreasing p with increasing wavelength), though the behavior is not strictly monotonic. The behavior of the far regime is distinct, with a median p that is approximately flat or increasing with wavelength.

Variations in polarization spectra have been seen across different clouds and environments before. Hildebrand et al. (1999) analyzed polarization spectra in molecular clouds with data from KAO and CSO at $60\ \mu\text{m}$, $100\ \mu\text{m}$, and $350\ \mu\text{m}$. They found that different environments of the cloud may have “rising” spectra that increase with wavelength, “flat” spectra that show no change with wavelength, or “falling” spectra that decrease with wavelength. Using data from KAO, CSO, the Submillimetre Common-User Bolometer Array (SCUBA) polarimeter on the James Clerk Maxwell Telescope (JCMT), Vaillancourt (2002) observed a V-shaped polarization spectrum where p decreases as a function of wavelength from $60\ \mu\text{m}$ to $350\ \mu\text{m}$, then increases towards longer wavelengths. The wavelength range in our paper covers the decreasing or falling part of the spectra observed in Vaillancourt (2002). Simulated polarization spectra have shown that the falling and V-shaped spectra can arise in sightlines where there are multiple dust populations with different temperatures along the line of sight (e.g., Lee et al. 2024; Seifried et al. 2025).

Observing the dependence of the polarization spectrum on cloud properties such as temperature (T) and column density (N_{H_2}) is a way to probe grain alignment mechanisms. Previous studies disagree on whether polarization spectra are primarily driven by T (e.g., Michail et al. 2021) or N_{H_2} (e.g., Hildebrand et al. 1999; Santos et al. 2019; Lee et al. 2024; Cox et al. 2025), with recent work frequently finding falling spectra in higher column density regions. Falling spectra in high-column-density regions may occur because dust grains in cold, dense environments self-shield from the radiation required for efficient grain alignment.

We look for evidence of a consistent dependence of polarization spectra on T or N_{H_2} by computing spectra that consist of data in certain T and N_{H_2} bins. We repeat this analysis for all of the data at $25''$, the close regime at $0.052\ \text{pc}$, and the far regime at $0.32\ \text{pc}$, as shown in Figure 7. It can be difficult to classify the shape of the spectra with only four wavelengths and varying degrees of spread around each me-

dian. We also do not necessarily expect the spectra to vary linearly, so defining the spectra with slopes may not fully capture their shape. Since we see qualitative similarities in the distributions of p between Bands A and C versus Bands D and E, we use the Cohen’s d statistic to assess whether the spectra are falling, flat, or rising. Cohen’s d is calculated as

$$d = \frac{\text{med}(p_{\text{short}}) - \text{med}(p_{\text{long}})}{\sigma_{\text{pooled}}}, \quad (10)$$

where $\text{med}(p_{\text{short}})$ is the median of the data in Bands A and C and $\text{med}(p_{\text{long}})$ is the median of the data in Bands D and E. We define

$$\sigma_{\text{pooled}} = \sqrt{\frac{\text{MAD}(p_{\text{short}})^2 + \text{MAD}(p_{\text{long}})^2}{2}}, \quad (11)$$

where $\text{MAD}(p_{\text{short}})$ and $\text{MAD}(p_{\text{long}})$ are the median absolute deviations (MAD) of the short and long wavelengths, respectively. We use the median and MAD to be consistent with previous polarization spectra analyses, and to prevent our results from being biased by outliers. With our sign convention, $d > 0$ is a falling spectrum and $d < 0$ is a rising spectrum. Following convention, we interpret $|d| \geq 0.8$ as a significant difference between the two groups of bands. We denote the calculated d in the legends of Figure 7.

Overall, we find that most bins in both T and N_{H_2} at all resolutions result in a $|d| < 0.8$, meaning we interpret most of our spectra as being consistent with flat. Notably, all N_{H_2} bins in the close regime at a resolution of $0.052\ \text{pc}$ have significant falling spectra. The lowest N_{H_2} bin in the far regime is also a significant rising spectrum. The only significant d we find in the T -binned spectra is in the lowest-temperature bin of the close regime. We find that there is more noticeably a trend in the shape and magnitude of the spectra with N_{H_2} , but no consistent trend with T . Generally, across all regimes, the high N_{H_2} bins have the lowest p , and the low N_{H_2} bins have the highest p , regardless of wavelength. However, when we bin the data by T , we do not see any qualitative trends.

Typical polarization spectra analyses are done with cuts to the data to only include sightlines with coverage in all wavelengths and that do not have large changes in the polarization angle with wavelength for a given sightline (e.g., Hildebrand et al. 1999; Vaillancourt 2002; Michail et al. 2021). However, in our data compilation we do not have uniform wavelength coverage in each region, and only have one wavelength for some regions. We devise a method to compute the polarization spectrum that is akin to having uniform wavelength coverage by sampling spectra from regions with identical properties in either T or N_{H_2} . Since Figure 7 shows a more consistent trend for the shape and magnitude of the spectra with N_{H_2} than T , we use N_{H_2} as our control variable and compute spectra where each wavelength has the same N_{H_2} distribution. Because Band A has the fewest sightlines, we use its N_{H_2} distribution as a control. We randomly sample (with replacement) half of the Band A measurements, then draw matching N_{H_2} distributions for the other bands to compute median p values. We do this resampling 1000 times

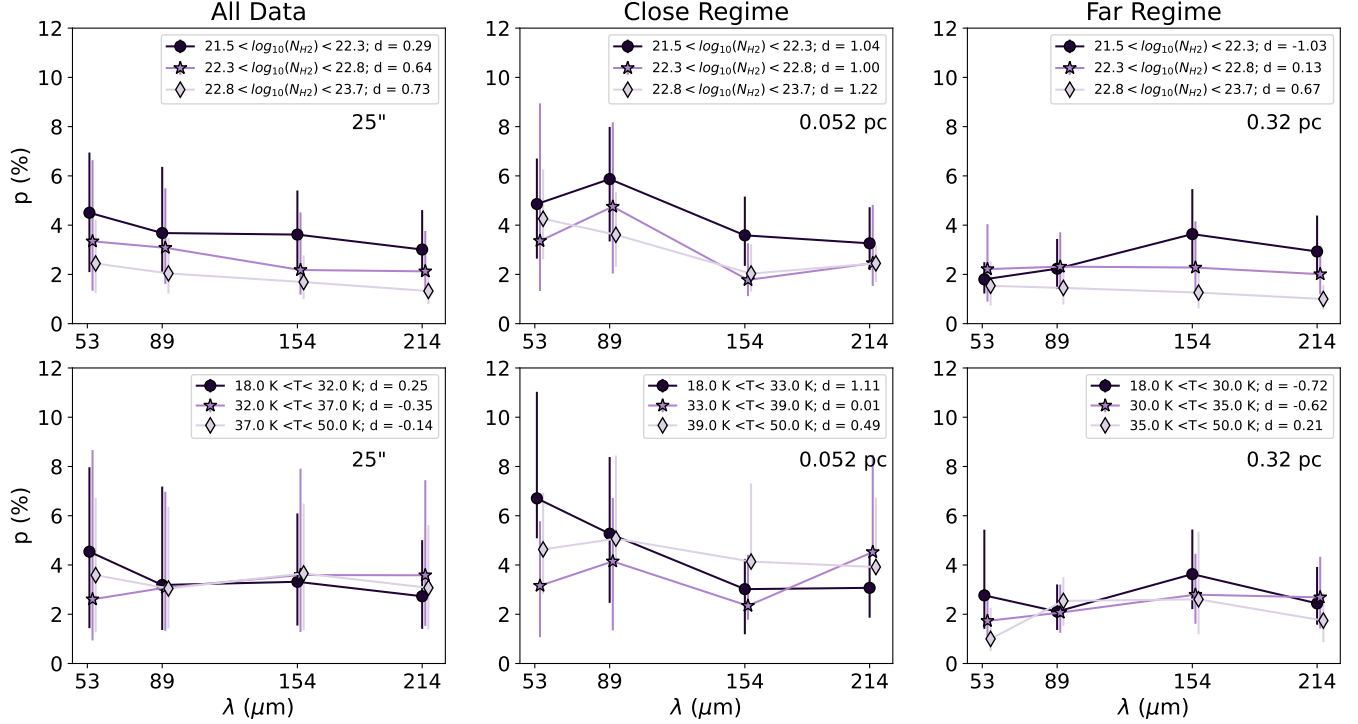


Figure 7. Polarization spectra created by separating the p data in N_{H_2} (Top) and T (Bottom) bins using circles, stars, and diamonds for the lowest, middle, and highest bins respectively. The error bars denote the first and third quartiles of the binned data. This is done for all of the data at a resolution of $25''$ (Left), the close regime at a resolution of 0.052 pc (Middle), and the far regime at a resolution of 0.32 pc (Right). The bins we use are denoted in the legends. We also denote the Cohen's d , calculated as defined in the text, of each spectrum in the legend

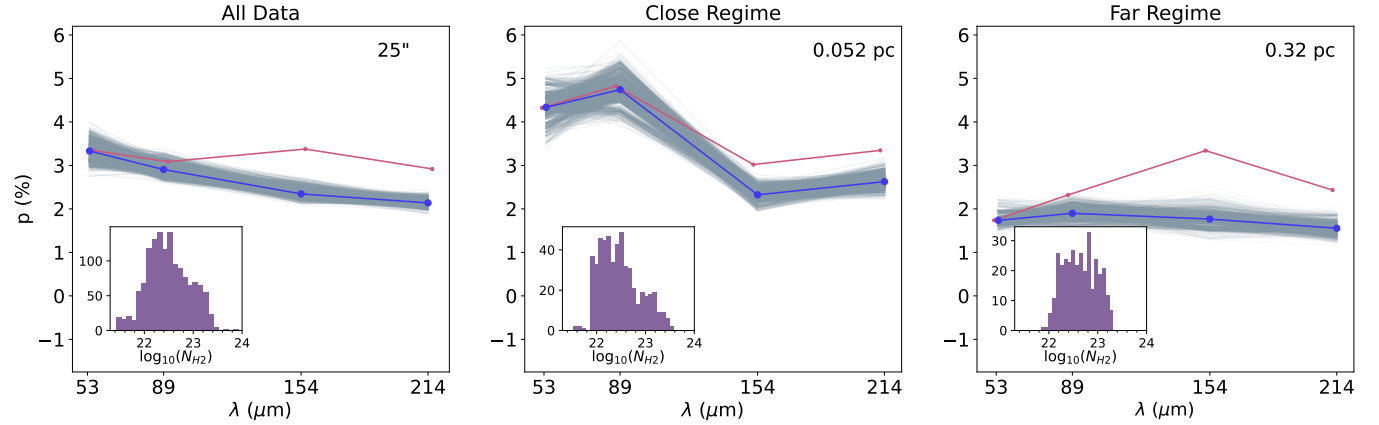


Figure 8. Polarization spectra computed over constant N_{H_2} distributions for all of the data (left), the close regime smoothed to 0.052 pc (middle), and the far regime smoothed to 0.32 pc (right). The blue spectra are the median p values of the 1000 samples. The grey lines show the p for each of the 1000 trials. The inset histograms show the distribution of N_{H_2} every band is fixed to. The pink data are the same as the common physical resolution data medians reported in Figure 6.

and compute the median of the samples. Figure 8 shows the spectra created using this method for all of the data, the close regime at a common physical resolution, and the far regime at a common physical resolution. We also show faint grey lines for the spectra created for all of the 1000 runs.

We find that computing spectra from the fixed N_{H_2} samples decreases p in the longer wavelengths compared to calculating the spectra from the full data. This could be because

we are fixing the N_{H_2} distribution to the Band A coverage, which tends to target the densest regions of the molecular clouds. High N_{H_2} portions of clouds have been observed to have systematically lower p (e.g., Fissel et al. 2016; Planck Collaboration et al. 2020b). We see generally consistent spectra across the 1000 samples of our data, as shown by the faint grey lines in Figure 8. We find a slight falling spectrum in all of the data at a resolution of $25''$, a more significant

falling spectrum in the close regime at a resolution of 0.052 pc, and a flat spectrum in the far regime at a resolution of 0.32 pc.

The transition from a falling spectrum in the close regime to the flat spectrum in the far regime may be caused by the physical scales resolved by our common physical resolutions. As noted above, the close regime is able to resolve smaller objects like cores and filaments. These are the denser regions of the clouds where we would expect falling spectra if, as argued in Cox et al. (2025), those spectra are caused by self-shielding in the colder grains. From our column density and temperature maps, we see that some of our regions have thin cold dense filaments and cores. In this picture, the resolution of the far regime is no longer able to resolve these small structures, and thus the observed polarization spectrum is flatter, and the polarization fraction is lower overall.

To confirm that the differences we are seeing between the close and far regime are not caused by different distributions of N_{H_2} in the different regimes, we repeat the same analysis for all of the data and the close regime after fixing to the N_{H_2} distribution of the far regime, and find that the spectra do not change significantly. Even though we see no trend in Figure 7 with T , we redo this analysis fixing to the Band A T distribution for all bands and find little difference between the fixed- T spectra and the spectra using all of the data. This confirms that we do not see a strong dependence on T with the polarization spectra of our data.

5.3. Magnetic Field Orientation

We analyze the magnetic field orientation in our regions in the context of larger-scale magnetic fields. In Figure 1 we show the average magnetic field orientation of each dataset. We calculate these orientations by computing the unweighted average of every sightline in the region that satisfies the signal-to-noise cuts described in Section 2.1. A preliminary comparison to the Planck 353 GHz polarization data in each individual region shows no obvious preferred relationship between the Planck-measured magnetic field orientation and the average HAWC+ magnetic field orientation. Our compilation could be used in conjunction with the Planck data to analyze magnetic fields across different spatial scales.

The large-scale Galactic magnetic field in the plane is expected to be parallel with the plane of a spiral galaxy like the Milky Way (e.g., Han et al. 2006). In agreement with this, Planck Collaboration et al. (2015b) found that the average dust polarization orientation in the Galactic plane corresponds to an angle of $\phi = 0^\circ$ ($\phi_B = 90^\circ$) in Galactic Coordinates. However, the dust polarization orientations in star-forming regions do not necessarily align with the Galactic plane (e.g., Planck Collaboration et al. 2015a; Stephens et al. 2011). The magnetic field of the Radcliffe Wave has been observed to be aligned with its structure, resulting in a magnetic field not aligned with the Galactic plane (Panopoulou et al. 2025). The cloud-scale magnetic fields may also become decoupled from the large-scale Galactic magnetic field during the formation of the cloud as it collapses, or from stellar feedback (Pattle et al. 2023).

The average magnetic field angles of our HAWC+ data reported in Figure 1 do not show a preferential alignment with $\phi_B = 90^\circ$, nor any other orientation. We also examine histograms of the magnetic field orientation (Figure 9). These histograms show no overdensity of measurements in the bins near $\phi_B = \pm 90^\circ$. We find no N_{H_2} dependence in the magnetic field orientation, indicating that even the lower N_{H_2} portions of the clouds we cover do not show increased influence from the large-scale Galactic magnetic field.

5.4. Depolarization and Column Density

We analyze the relationship between p and N_{H_2} in the close (Figure 10) and far (Figure 11) regimes using 2-dimensional histograms. Before plotting, we Nyquist sample the data to avoid the appearance of trends from oversampling the beam. We show the fifth percentile, median, and ninety-fifth percentiles as solid magenta lines and report the Spearman ρ value for the data in each plot in Figure 10 and Figure 11. In both the close and far regimes, we broadly see a negative correlation denoted by the calculated Spearman ρ in the range -0.04 to -0.46 , but we do not see any very strong negative relationships of Spearman $\rho \leq -0.5$. In the close regime (Figure 10), the most significant relationship we see occurs in Band D, with $\rho \sim -0.4$. In the far regime (Figure 11), we see the most negative relationships in Bands D and E at both resolutions, also with $\rho \sim -0.4$.

Bands A and C generally have the least significant ρ values, except for Band C in the close regime at the common angular resolution (Figure 10). The ninety-fifth percentiles at higher N_{H_2} ($\sim 10^{23} \text{ cm}^{-2}$), especially in the common angular resolution data, are also generally higher in Bands A and C than in Bands D and E. This implies that warm dust grains have less depolarization in high N_{H_2} regions.

The dust polarization fraction and N_{H_2} have been observed to have an inverse relationship in molecular clouds at longer wavelengths (e.g., 250 – 850 μm ; Planck Collaboration et al. 2020a; Fissel et al. 2016). We note that our longest wavelengths, especially in the far regime, have the strongest negative correlations, implying that there may be a wavelength dependence to this correlation strength. This decrease in polarization efficiency in high N_{H_2} regions may be expected for a few reasons, such as collisions between dust grains and gas being more common in these dense regions, causing them to become unaligned (Reissl et al. 2020), the coagulation of icy materials onto the dust grains giving them less elongated shapes and decreasing their propensity for magnetic alignment (Juárez et al. 2017), and the shielding of radiation preventing the grains from being efficiently radiatively torqued (Hildebrand et al. 1999). This depolarization may also be caused if the magnetic field is more tangled at high column density (Falseta-Gonçalves et al. 2008).

Planck Collaboration et al. (2020a) found that individual datasets showed different relationships between p and N_{H_2} , so we analyze the $p - N_{H_2}$ correlation in each individual dataset. Figure 12 shows a histogram of the Spearman ρ coefficients of the individual datasets smoothed to the common angular resolution. We find that for the common angular res-

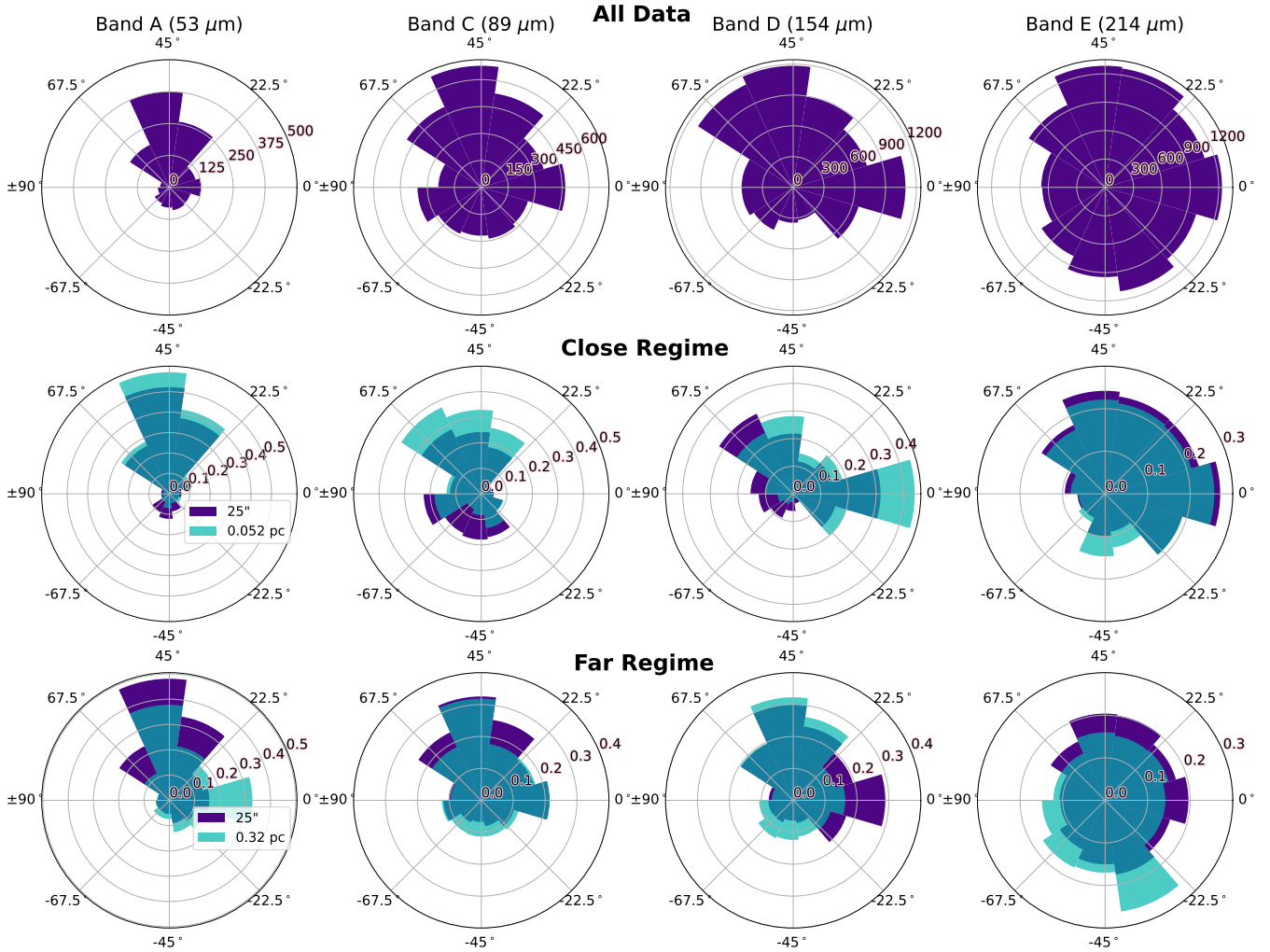


Figure 9. Histograms of the of magnetic field pseudovector orientations (ϕ_B) in Galactic coordinates. The half-polar polarization data are wrapped onto a full polar plot so that the orientations $+90^\circ$ and -90° are in the same location. An orientation of 0° is oriented toward Galactic north. *Top:* All of the data smoothed to $25''$. *Middle:* Density histograms of the data in the close regime smoothed to $25''$ (purple) and smoothed to 0.052 parsec (cyan). *Bottom:* Density histograms of the data in the close regime smoothed to $25''$ (purple) and smoothed to 0.32 parsec (cyan)

olution, 53% of the close regime datasets and 64% of the far regime regions have significant negative correlations of $\rho < -0.5$. For the common physical resolution we find that 44% of datasets in the close regime and 64% of datasets in the far regime have significant negative correlations. To estimate uncertainty on ρ , we resample the data with replacement 500 times to estimate the 95% confidence intervals. We find that the median widths of these confidence intervals are 0.13 (close common angular), 0.12 (far common angular), 0.18 (close common physical), and 0.27 (far common physical). Using the higher and lower limits of the confidence interval, we find that 41% – 59% (close common angular), 45% – 80% (far common angular), 28% – 56% (close common physical), and 40% – 89% (far common physical) satisfy $\rho < -0.5$.

Figure 12 shows that over half of the regions in both regimes have $\rho < -0.5$. Even conservatively using the upper limits of the confidence intervals, we would conclude that a

significant fraction of the regions have this strong negative correlation. Just as in the aggregate data, Bands D and E show the strongest $p - N_{H_2}$ anticorrelations, and Bands A and C show the weakest.

We consider whether the datasets with significant $p - N_{H_2}$ anticorrelations also display strong $S - N_{H_2}$ correlations, as might be expected if the $p - N_{H_2}$ relationship is driven by geometric depolarization in high N_{H_2} regions. This is not clearly supported by the data, however; we find that at the common angular resolution, only 11% (close regime) and 36% (far regime) of the datasets with significant $p - N_{H_2}$ anticorrelations also display significant $S - N_{H_2}$ correlations. The mechanisms that drive depolarization may therefore be complex, or variable across regions and/or wavelengths.

5.5. Depolarization and Angular Dispersion

We investigate the distributions of S . In Figure 5, we show the distributions of S when calculated using radii of $1, \frac{3}{2}$,

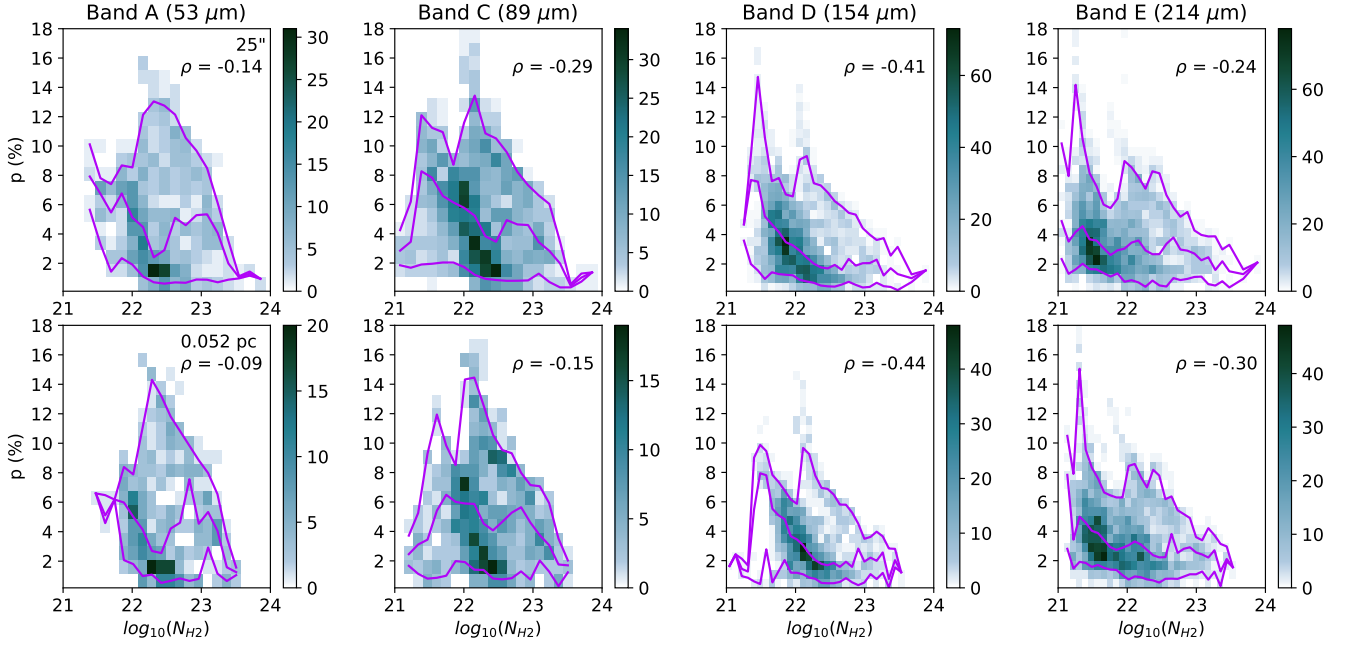


Figure 10. 2D histograms of the percent polarization vs the column density across the four HAWC+ bands for the close regime smoothed to $25''$ (top) and 0.052 pc bottom. The three purple lines from bottom to top are the fifth percentile, median, and ninety-fifth percentile. The Spearman ρ coefficient of the data is reported on each plot to quantify the inverse relationship.

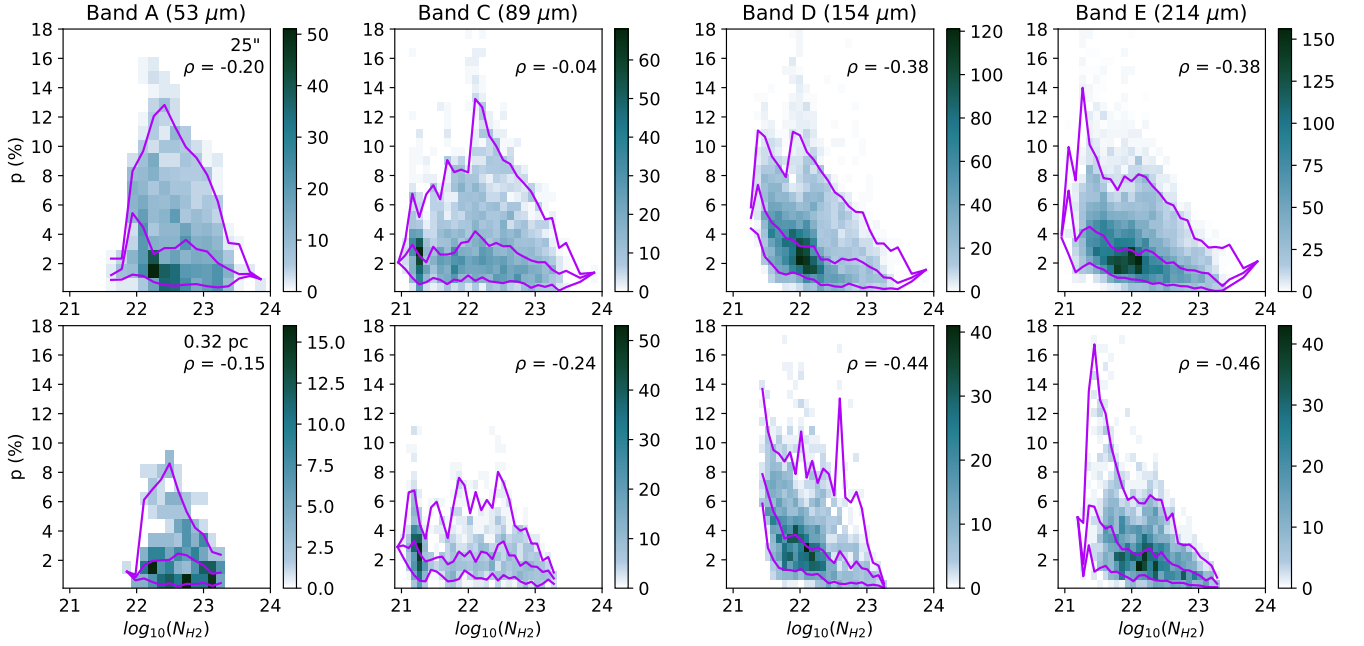


Figure 11. The same as Figure 10 but for the far regime. The bottom row is smoothed to 0.32 pc.

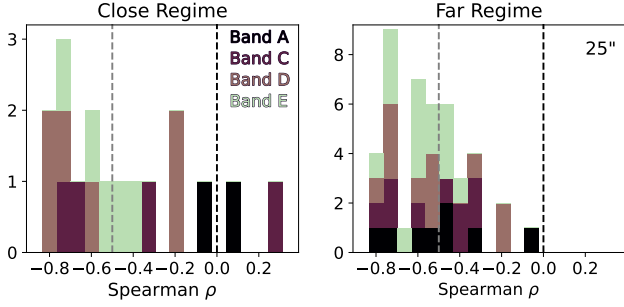


Figure 12. Stacked histograms of the Spearman ρ coefficients between p and N_{H_2} for the individual datasets separated into the close (left) and far (right) regimes at the common angular resolution. The data in each band are stacked and are colored blue, green, orange, and red for Bands A, C, D, and E respectively. The grey dashed line is at $\rho = -0.5$ and the black dashed line is at $\rho = 0$.

and 2 beams for data smoothed to the common angular and physical resolutions. The medians of the distributions of S all increase as the radius S is calculated over increases. This implies that there are larger magnetic field fluctuations on scales larger than one beam. This trend is seen in both the close and far regime, meaning S seems to increase from scales ~ 0.1 pc to ~ 1 pc. The common angular resolution data in the far regime has higher dispersion than the close regime, which is consistent with the general decrease in p observed when the far regime data were smoothed to the common physical resolution.

In molecular clouds, p and S have been observed to have an inverse power law relationship that is consistent across different regions (e.g., Planck Collaboration et al. 2020a; Chuss et al. 2019; Fissel et al. 2016). Power law fits in Chuss et al. (2019) and Fissel et al. (2016) find indices between -0.67 and -0.9. Planck Collaboration et al. (2020a) derived a power law index for an inverse relationship entirely caused by beam depolarization of -1 (Planck Collaboration et al. 2020a, Appendix F.6). We show 2-D histograms of p as a function of S in Figure 13 with the fifth percentile, median, and ninety-fifth percentiles as solid magenta lines. We fit our data with a power law,

$$p = CS^\alpha. \quad (12)$$

Because the power-law relationship breaks down and p flattens at low S , we exclude data where $S < 2^\circ$. The results of the fit are reported in Figure 13.

We find significant inverse relationships with our data at all wavelengths and resolutions. We expect an inverse relationship between p and S due to this beam depolarization effect. In Figure 13, we show our distribution of p versus S and see that our indices range from -0.51 to -0.85, consistent with previous studies. The $p - S$ correlation is uniformly negative, and more consistent across regions than the $p - N_{H_2}$ correlation.

At the common angular resolution, Bands A and C have the lowest indices and strongest negative correlation (Spearman $\rho \sim 0.8$). This contrasts with the observation that the

shorter wavelengths had the least significant correlation between p and N_{H_2} (Section 5.4). Overall, p shows a stronger negative correlation with S than N_{H_2} , meaning a significant amount of the depolarization is likely from beam depolarization. When smoothed to the common physical resolution, there is not much change in the indices or Spearman ρ values in the close regime. However, in the far regime the scatter in Bands A and C increases and ρ becomes less significant. We note that the inclination angle between the mean magnetic field and the line of sight also affects the $p - S$ correlation (e.g., King et al. 2018), but the uniformity of α across our sample suggests that inclination effects are not the dominant driver of this correlation slope, as we do not expect every region to have the same mean magnetic field inclination angle.

6. CONCLUSIONS

We present archival polarization data from the HAWC+ instrument on SOFIA toward 26 nearby star-forming regions. Far-infrared data from the PACS and SPIRE instruments on the Herschel Space Observatory are used to derive maps of column density (N_{H_2}) and temperature (T). We analyze trends in the polarization data as a function of wavelength, and the relationship between the dust polarization fraction and N_{H_2} , T , and polarization angle dispersion (S). By analyzing these trends at both a common angular resolution (25'') and common physical resolutions (0.052 pc and 0.32 pc), we come to the following conclusions:

1. We find that the two shortest wavelengths of HAWC+ (53 μm and 89 μm) exhibit qualitatively distinct properties from the two longer wavelengths. At the common angular resolution, we find that p is significantly affected by the cloud distance, with the p distribution skewed toward higher values for more nearby regions. The shorter wavelengths have wider distributions of p than the longer wavelengths, and smoothing to the common physical resolution decreases p more in the shorter wavelengths. We interpret this as evidence that the shorter wavelengths are sensitive to a distinct dust population: likely warmer grains that may not be spatially co-located with cooler dust populations.
2. When binned by N_{H_2} and T , the shape and magnitude of the polarization spectra calculated from our compilation show a more consistent dependence on N_{H_2} than T . We create polarization spectra with identical distributions of N_{H_2} to control for polarization effects that are correlated with N_{H_2} . We find a falling spectrum (decreasing with increasing wavelength) when analyzing the data at 0.052 pc, but a flat spectrum at 0.32 pc. The falling spectrum in the close regime can be from environmental factors such as shielding of colder grains, or it can be from beam depolarization in these shortest wavelengths.
3. We find no preferred alignment between the mean plane-of-sky magnetic field in our regions and the

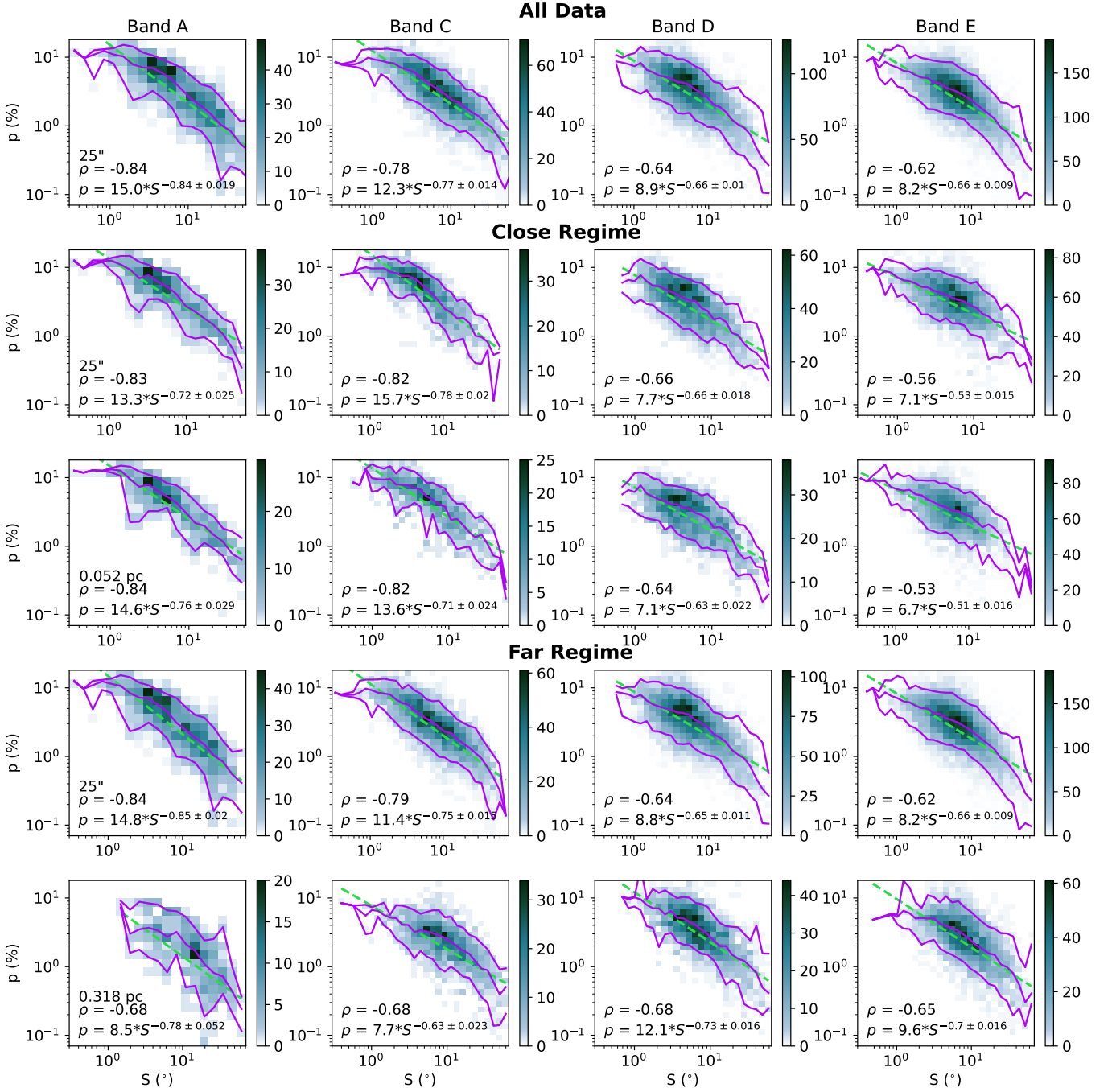


Figure 13. 2-D histograms of p as a function of S separated by HAWC+ band. The three purple lines from bottom to top are the fifth percentile, median, and ninety-fifth percentile. The dashed green line shows the power law fit described in Section 5.5. The fit equation and Spearman ρ are denoted on each subplot.

Galactic plane. Assuming that the large-scale Galactic magnetic field is parallel to the Galactic plane, our findings imply that the magnetic fields in the star-forming regions we analyze are decoupled from the large-scale Galactic magnetic field.

4. When looking at all the data in each distance regime combined, we consistently see a negative trend between p and N_{H_2} , but we do not see any highly significant anticorrelations. However, we do find some significant correlations (Spearman $\rho \leq -0.5$) between these parameters in individual data sets. The individual $p - N_{H_2}$ correlations are not as uniform across regions as the $p - S$ correlations. There can be variations between clouds in their geometry, magnetic field structure, or dust properties that may affect the relationship between depolarization and column density, making it important to explore the physics of these clouds independently.
5. In contrast, the negative relationship between p and S is evident across all wavelengths and resolutions and is a quite consistent trend, with all the data generally falling along one curve. This likely means that beam depolarization is generally a stronger source of depolarization than effects related to N_{H_2} . We fit a power law to our data and find indices in the range -0.51 to -0.84, with the steepest indices tending to fit the Bands A and C data.

Our compilation enables statistical investigations of dust polarization properties in star-forming regions across far-infrared wavelengths. Our results illustrate the importance of observing star-forming regions at both shorter wavelengths ($\lesssim 100 \mu\text{m}$) and longer wavelengths ($\gtrsim 100 \mu\text{m}$) and re-

solving sub-parsec structures in the dust polarization in order to interpret the observations. Future far-infrared instruments such as PRIMA (Glenn et al. 2025), with its instrument PRIMAgger (Ciesla et al. 2025), will be an excellent tool for measuring dust polarization in molecular clouds, with similar resolution and higher sensitivity than HAWC+. PRIMA can be used to analyze a broader range of Galactic environments and the connection between these dense, small scale portions of clouds and larger, more diffuse cloud environments.

1 We thank Laura Fissel for helpful discussions that improved
2 this paper.

3 Based on observations made with the NASA/DLR Strato-
4 spheric Observatory for Infrared Astronomy (SOFIA).
5 SOFIA is jointly operated by the Universities Space Re-
6 search Association, Inc. (USRA), under NASA contract
7 NNA17BF53C, and the Deutsches SOFIA Institut (DSI) un-
8 der DLR contract 50 OK 2002 to the University of Stuttgart.

9 This work was supported by NASA award
10 80NSSC23K0972. S.E.C. additionally acknowledges sup-
11 port from an Alfred P. Sloan Research Fellowship.

12 E.L.-R. thanks to the support of the NASA Astro-
13 physics Decadal Survey Precursor Science (ADSPS) Pro-
14 gram (NNH22ZDA001N-ADSPS) with ID 22-ADSPS22-
15 0009 and agreement number 80NSSC23K1585.

16 Some of the computing for this project was performed on
17 the Sherlock cluster. We would like to thank Stanford Uni-
18 versity and the Stanford Research Computing Center for pro-
19 viding computational resources and support that contributed
20 to these research results.

Facilities: SOFIA, Herschel

Software: Astropy (Astropy Collaboration et al. 2013, 2018, 2022), emcee (Foreman-Mackey et al. 2013), Matplotlib (Hunter 2007), SciPy (Virtanen et al. 2020)

APPENDIX

A.1. SUPPLEMENTARY MATERIALS

In Figure A.1, we show the remaining HAWC+ maps with inferred magnetic field pseudovectors that were not included in Figure 2 or Figure 3. Table A.1 details information about each of the HAWC+ observations we use for our analyses. We include the available bands, the plan IDs, the original proposal PIs, the exposure time, the chop angles and amplitudes, the SOFIA Redux versions used to reduce the data, and the first publications to use the data.

REFERENCES

- André, P., Men'shchikov, A., Bontemps, S., et al. 2010, *A&A*, 518, L102, doi: [10.1051/0004-6361/201014666](https://doi.org/10.1051/0004-6361/201014666)
- Arzoumanian, D., André, P., Didelon, P., et al. 2011, *A&A*, 529, L6, doi: [10.1051/0004-6361/201116596](https://doi.org/10.1051/0004-6361/201116596)
- Ashton, P. C., Ade, P. A. R., Angilè, F. E., et al. 2018, *ApJ*, 857, 10, doi: [10.3847/1538-4357/aab3ca](https://doi.org/10.3847/1538-4357/aab3ca)
- Astropy Collaboration, Robitaille, T. P., Tollerud, E. J., et al. 2013, *A&A*, 558, A33, doi: [10.1051/0004-6361/201322068](https://doi.org/10.1051/0004-6361/201322068)
- Astropy Collaboration, Price-Whelan, A. M., Sipőcz, B. M., et al. 2018, *AJ*, 156, 123, doi: [10.3847/1538-3881/aabc4f](https://doi.org/10.3847/1538-3881/aabc4f)
- Astropy Collaboration, Price-Whelan, A. M., Lim, P. L., et al. 2022, *ApJ*, 935, 167, doi: [10.3847/1538-4357/ac7c74](https://doi.org/10.3847/1538-4357/ac7c74)

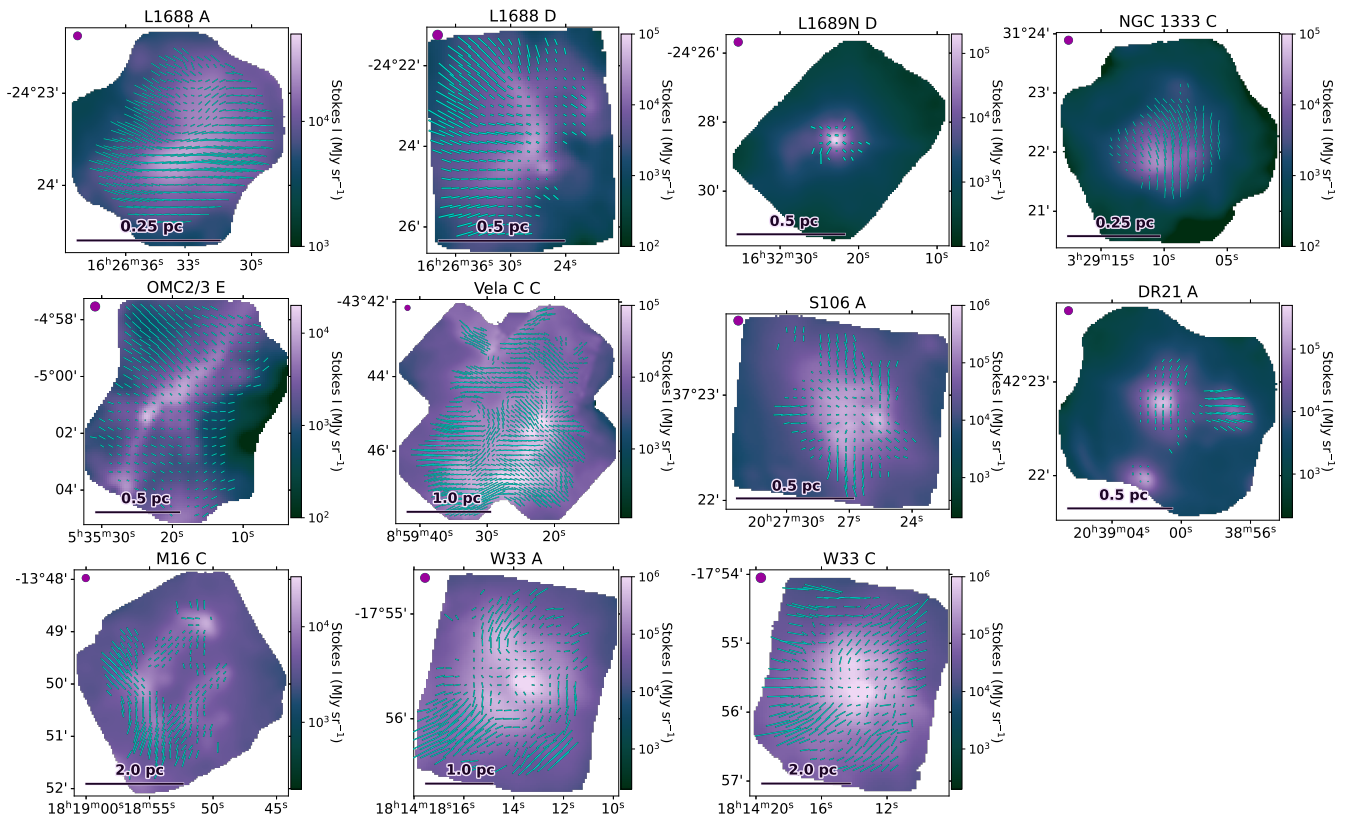


Figure A.1. Remaining HAWC+ dataset that are not shown in Figure 2 or Figure 3.

- Barnes, P. J., Ryder, S. D., Novak, G., et al. 2023, *ApJ*, 945, 34, doi: [10.3847/1538-4357/acac27](https://doi.org/10.3847/1538-4357/acac27)
- Barnes, P. J., Ryder, S. D., Novak, G., & Fissel, L. M. 2025, *The Magnetic Keys to Massive Star Formation: The Western η Carinae Giant Molecular Cloud*. <https://arxiv.org/abs/2504.17842>
- Barnes, P. J., Yonekura, Y., Ryder, S. D., et al. 2010, *Monthly Notices of the Royal Astronomical Society*, 402, 73, doi: [10.1111/j.1365-2966.2009.15890.x](https://doi.org/10.1111/j.1365-2966.2009.15890.x)
- Bethell, T. J., Chepurnov, A., Lazarian, A., & Kim, J. 2007, *The Astrophysical Journal*, 663, 1055, doi: [10.1086/516622](https://doi.org/10.1086/516622)
- Bij, A., Fissel, L. M., Bonne, L., et al. 2024, *ApJ*, 975, 267, doi: [10.3847/1538-4357/ad77c7](https://doi.org/10.3847/1538-4357/ad77c7)
- Cesaroni, R. 2005, *Proceedings of the International Astronomical Union*, 1, 59–69, doi: [10.1017/S1743921305004369](https://doi.org/10.1017/S1743921305004369)
- Chuss, D. T., Andersson, B. G., Bally, J., et al. 2019, *ApJ*, 872, 187, doi: [10.3847/1538-4357/aaf37](https://doi.org/10.3847/1538-4357/aaf37)
- Ciesla, L., Dowell, C. D., Sauvage, M., et al. 2025, *Journal of Astronomical Telescopes, Instruments, and Systems*, 11, 031625, doi: [10.1117/1.JATIS.11.3.031625](https://doi.org/10.1117/1.JATIS.11.3.031625)
- Córdova Rosado, R., Hensley, B. S., Clark, S. E., et al. 2024, *ApJ*, 960, 96, doi: [10.3847/1538-4357/ad05cd](https://doi.org/10.3847/1538-4357/ad05cd)
- Coudé, S., Stephens, I. W., Myers, P. C., et al. 2025, *The Astrophysical Journal Supplement Series*, 282, 2, doi: [10.3847/1538-4365/ae0e61](https://doi.org/10.3847/1538-4365/ae0e61)
- Cox, E. G., Novak, G., Chuss, D. T., et al. 2025, *ApJ*, 981, 132, doi: [10.3847/1538-4357/ada447](https://doi.org/10.3847/1538-4357/ada447)
- Davis, Jr., L., & Greenstein, J. L. 1951, *ApJ*, 114, 206, doi: [10.1086/145464](https://doi.org/10.1086/145464)
- Dolginov, A. Z., & Mitrofanov, I. G. 1976, *Ap&SS*, 43, 291, doi: [10.1007/BF00640010](https://doi.org/10.1007/BF00640010)
- Dowell, C. D. 1997, *ApJ*, 487, 237, doi: [10.1086/304577](https://doi.org/10.1086/304577)
- Dowell, C. D., Hildebrand, R. H., Schleuning, D. A., et al. 1998, *ApJ*, 504, 588, doi: [10.1086/306069](https://doi.org/10.1086/306069)
- Draine, B. T. 2006, *The Astrophysical Journal*, 636, 1114, doi: [10.1086/498130](https://doi.org/10.1086/498130)
- Draine, B. T., & Hensley, B. S. 2021, *The Astrophysical Journal*, 909, 94, doi: [10.3847/1538-4357/abd6c6](https://doi.org/10.3847/1538-4357/abd6c6)
- Draine, B. T., & Weingartner, J. C. 1997, *ApJ*, 480, 633, doi: [10.1086/304008](https://doi.org/10.1086/304008)
- Díaz-Márquez, E., Grau, R., Busquet, G., et al. 2023, *Radio survey of the stellar population in the infrared dark cloud G14.225-0.506*. <https://arxiv.org/abs/2311.12542>
- Encalada, F. J., Looney, L. W., Novak, G., et al. 2024, *ApJ*, 968, 101, doi: [10.3847/1538-4357/ad4968](https://doi.org/10.3847/1538-4357/ad4968)
- Falceta-Gonçalves, D., Lazarian, A., & Kowal, G. 2008, *ApJ*, 679, 537, doi: [10.1086/587479](https://doi.org/10.1086/587479)
- Federrath, C., & Klessen, R. S. 2012, *ApJ*, 761, 156, doi: [10.1088/0004-637X/761/2/156](https://doi.org/10.1088/0004-637X/761/2/156)

- Fedriani, R., Tan, J. C., Telkamp, Z., et al. 2022, *The Astrophysical Journal*, 942, 7, doi: [10.3847/1538-4357/aca4cf](https://doi.org/10.3847/1538-4357/aca4cf)
- Fernández-López, M., Arce, H. G., Looney, L., et al. 2014, *The Astrophysical Journal Letters*, 790, L19, doi: [10.1088/2041-8205/790/2/L19](https://doi.org/10.1088/2041-8205/790/2/L19)
- Fissel, L. M., Ade, P. A. R., Angilè, F. E., et al. 2016, *ApJ*, 824, 134, doi: [10.3847/0004-637X/824/2/134](https://doi.org/10.3847/0004-637X/824/2/134)
- Fissel, L. M., Ade, P. A. R., Angilè, F. E., et al. 2019, *The Astrophysical Journal*, 878, 110, doi: [10.3847/1538-4357/ab1eb0](https://doi.org/10.3847/1538-4357/ab1eb0)
- Foreman-Mackey, D., Hogg, D. W., Lang, D., & Goodman, J. 2013, *PASP*, 125, 306, doi: [10.1086/670067](https://doi.org/10.1086/670067)
- Friesen, R. K., Johnstone, D., Naylor, D. A., & Davis, G. R. 2005, *MNRAS*, 361, 460, doi: [10.1111/j.1365-2966.2005.09179.x](https://doi.org/10.1111/j.1365-2966.2005.09179.x)
- Glenn, J., Meixner, M., Bradford, C. M., et al. 2025, *Journal of Astronomical Telescopes, Instruments, and Systems*, 11, 031628, doi: [10.1117/1.JATIS.11.3.031628](https://doi.org/10.1117/1.JATIS.11.3.031628)
- Griffin, M. J., Abergel, A., Abreu, A., et al. 2010, *A&A*, 518, L3, doi: [10.1051/0004-6361/201014519](https://doi.org/10.1051/0004-6361/201014519)
- Hacar, A., Tafalla, M., Kauffmann, J., & Kovács, A. 2013, *A&A*, 554, A55, doi: [10.1051/0004-6361/201220090](https://doi.org/10.1051/0004-6361/201220090)
- Han, J. L., Manchester, R. N., Lyne, A. G., Qiao, G. J., & van Straten, W. 2006, *ApJ*, 642, 868, doi: [10.1086/501444](https://doi.org/10.1086/501444)
- Harper, D. A., Runyan, M. C., Dowell, C. D., et al. 2018, *Journal of Astronomical Instrumentation*, 7, 1840008, doi: [10.1142/S2251171718400081](https://doi.org/10.1142/S2251171718400081)
- Hennemann, M., Motte, F., Schneider, N., et al. 2012, *A&A*, 543, L3, doi: [10.1051/0004-6361/201219429](https://doi.org/10.1051/0004-6361/201219429)
- Hensley, B. S., & Draine, B. T. 2021, *ApJ*, 906, 73, doi: [10.3847/1538-4357/abc8f1](https://doi.org/10.3847/1538-4357/abc8f1)
- Hildebrand, R., Davidson, J., Dotson, J., et al. 2000, *Publications of the Astronomical Society of the Pacific*, 112, 1215
- Hildebrand, R. H., Dotson, J. L., Dowell, C. D., Schleuning, D. A., & Vaillancourt, J. E. 1999, *The Astrophysical Journal*, 516, 834, doi: [10.1086/307142](https://doi.org/10.1086/307142)
- Hoang, T. D., Ngoc, N. B., Diep, P. N., et al. 2022, *ApJ*, 929, 27, doi: [10.3847/1538-4357/ac5abf](https://doi.org/10.3847/1538-4357/ac5abf)
- Hunter, J. D. 2007, *Computing in Science & Engineering*, 9, 90, doi: [10.1109/MCSE.2007.55](https://doi.org/10.1109/MCSE.2007.55)
- Hunter, T. R. 1998, *PASP*, 110, 634, doi: [10.1086/316163](https://doi.org/10.1086/316163)
- Immer, K., Reid, M. J., Menten, K. M., Brunthaler, A., & Dame, T. M. 2013, *A&A*, 553, A117, doi: [10.1051/0004-6361/201220793](https://doi.org/10.1051/0004-6361/201220793)
- Juárez, C., Girart, J. M., Frau, P., et al. 2017, *A&A*, 597, A74, doi: [10.1051/0004-6361/201628608](https://doi.org/10.1051/0004-6361/201628608)
- King, P. K., Fissel, L. M., Chen, C.-Y., & Li, Z.-Y. 2018, *MNRAS*, 474, 5122, doi: [10.1093/mnras/stx3096](https://doi.org/10.1093/mnras/stx3096)
- Kounkel, M., Hartmann, L., Loinard, L., et al. 2017, *The Astrophysical Journal*, 834, 142, doi: [10.3847/1538-4357/834/2/142](https://doi.org/10.3847/1538-4357/834/2/142)
- Krumholz, M. R., & Tan, J. C. 2007, *ApJ*, 654, 304, doi: [10.1086/509101](https://doi.org/10.1086/509101)
- Kuhn, M. A., Hillenbrand, L. A., Sills, A., Feigelson, E. D., & Getman, K. V. 2019, *The Astrophysical Journal*, 870, 32, doi: [10.3847/1538-4357/aaef8c](https://doi.org/10.3847/1538-4357/aaef8c)
- Kurayama, T., Nakagawa, A., Sawada-Satoh, S., et al. 2011, *Publications of the Astronomical Society of Japan*, 63, 513–525, doi: [10.1093/pasj/63.3.513](https://doi.org/10.1093/pasj/63.3.513)
- Lazarian, A., & Hoang, T. 2007, *MNRAS*, 378, 910, doi: [10.1111/j.1365-2966.2007.11817.x](https://doi.org/10.1111/j.1365-2966.2007.11817.x)
- Lee, D., Berthoud, M., Chen, C.-Y., et al. 2021, *ApJ*, 918, 39, doi: [10.3847/1538-4357/ac0cf2](https://doi.org/10.3847/1538-4357/ac0cf2)
- Lee, D., Chen, C.-Y., Novak, G., et al. 2024, *ApJ*, 972, 102, doi: [10.3847/1538-4357/ad631c](https://doi.org/10.3847/1538-4357/ad631c)
- Lopez-Rodriguez, E., Clarke, M., Shenoy, S., et al. 2022, *ApJ*, 936, 65, doi: [10.3847/1538-4357/ac83ac](https://doi.org/10.3847/1538-4357/ac83ac)
- Mac Low, M.-M., & Klessen, R. S. 2004, *Reviews of Modern Physics*, 76, 125, doi: [10.1103/RevModPhys.76.125](https://doi.org/10.1103/RevModPhys.76.125)
- Michail, J. M., Ashton, P. C., Berthoud, M. G., et al. 2021, *ApJ*, 907, 46, doi: [10.3847/1538-4357/abd090](https://doi.org/10.3847/1538-4357/abd090)
- Mouschovias, T. C., & Spitzer, Jr., L. 1976, *ApJ*, 210, 326, doi: [10.1086/154835](https://doi.org/10.1086/154835)
- Müller, T., Okumura, K., & Klaas, U. 2011, *PACS Photometer Passbands and Colour Correction Factors for Various Source SEDs*, <https://www.cosmos.esa.int/documents/12133/996891/PACS+Photometer+Passbands+and+Colour+Correction+Factors+for+Various+Source+SEDs>
- Navarete, F., Galli, P. A. B., & Daminieli, A. 2019, *Monthly Notices of the Royal Astronomical Society*, 487, 2771–2784, doi: [10.1093/mnras/stz1442](https://doi.org/10.1093/mnras/stz1442)
- Ortiz-León, G. N., Loinard, L., Kounkel, M. A., et al. 2017, *The Astrophysical Journal*, 834, 141, doi: [10.3847/1538-4357/834/2/141](https://doi.org/10.3847/1538-4357/834/2/141)
- Ortiz-León, G. N., Loinard, L., Dzib, S. A., et al. 2018, *The Astrophysical Journal Letters*, 869, L33, doi: [10.3847/2041-8213/aaf6ad](https://doi.org/10.3847/2041-8213/aaf6ad)
- Panopoulou, G. V., Clark, S. E., Hacar, A., et al. 2022, *A&A*, 657, L13, doi: [10.1051/0004-6361/202142281](https://doi.org/10.1051/0004-6361/202142281)
- Panopoulou, G. V., Zucker, C., Clemens, D., et al. 2025, *A&A*, 694, A97, doi: [10.1051/0004-6361/202450991](https://doi.org/10.1051/0004-6361/202450991)
- Pattle, K., Fissel, L., Tahani, M., Liu, T., & Ntormousi, E. 2023, in *Astronomical Society of the Pacific Conference Series*, Vol. 534, *Protostars and Planets VII*, ed. S. Inutsuka, Y. Aikawa, T. Muto, K. Tomida, & M. Tamura, 193, doi: [10.48550/arXiv.2203.11179](https://doi.org/10.48550/arXiv.2203.11179)
- Pillai, T. G. S., Clemens, D. P., Reissl, S., et al. 2020, *Nature Astronomy*, 4, 1195, doi: [10.1038/s41550-020-1172-6](https://doi.org/10.1038/s41550-020-1172-6)
- Planck Collaboration, Ade, P. A. R., Aghanim, N., et al. 2015a, *A&A*, 576, A104, doi: [10.1051/0004-6361/201424082](https://doi.org/10.1051/0004-6361/201424082)
- . 2015b, *A&A*, 576, A104, doi: [10.1051/0004-6361/201424082](https://doi.org/10.1051/0004-6361/201424082)
- . 2016, *A&A*, 586, A138, doi: [10.1051/0004-6361/201525896](https://doi.org/10.1051/0004-6361/201525896)

- Planck Collaboration, Aghanim, N., Akrami, Y., et al. 2020a, *A&A*, 641, A12, doi: [10.1051/0004-6361/201833885](https://doi.org/10.1051/0004-6361/201833885)
- Planck Collaboration, Aghanim, N., Akrami, Y., et al. 2020b, *A&A*, 641, A3, doi: [10.1051/0004-6361/201832909](https://doi.org/10.1051/0004-6361/201832909)
- Planck Collaboration, Akrami, Y., Ashdown, M., et al. 2020c, *A&A*, 641, A11, doi: [10.1051/0004-6361/201832618](https://doi.org/10.1051/0004-6361/201832618)
- Plaszczynski, S., Montier, L., Levrier, F., & Tristram, M. 2014, *MNRAS*, 439, 4048, doi: [10.1093/mnras/stu270](https://doi.org/10.1093/mnras/stu270)
- Platt, S. R., Hildebrand, R. H., Pernic, R. J., Davidson, J. A., & Novak, G. 1991, *PASP*, 103, 1193, doi: [10.1086/132940](https://doi.org/10.1086/132940)
- Poglitich, A., Waelkens, C., Geis, N., et al. 2010, *A&A*, 518, L2, doi: [10.1051/0004-6361/201014535](https://doi.org/10.1051/0004-6361/201014535)
- Reissl, S., Guillet, V., Brauer, R., et al. 2020, *A&A*, 640, A118, doi: [10.1051/0004-6361/201937177](https://doi.org/10.1051/0004-6361/201937177)
- Reyes-Reyes, S. D., Stutz, A. M., Megeath, S. T., et al. 2024, *Monthly Notices of the Royal Astronomical Society*, 529, 2220, doi: [10.1093/mnras/stae631](https://doi.org/10.1093/mnras/stae631)
- Roccatagliata, V., Franciosini, E., Sacco, G. G., Randich, S., & Sicilia-Aguilar, A. 2020, *A&A*, 638, A85, doi: [10.1051/0004-6361/201936401](https://doi.org/10.1051/0004-6361/201936401)
- Rygl, K. L. J., Brunthaler, A., Sanna, A., et al. 2012, *Astronomy & Astrophysics*, 539, A79, doi: [10.1051/0004-6361/201118211](https://doi.org/10.1051/0004-6361/201118211)
- Sadavoy, S. I., Di Francesco, J., Johnstone, D., et al. 2013, *ApJ*, 767, 126, doi: [10.1088/0004-637X/767/2/126](https://doi.org/10.1088/0004-637X/767/2/126)
- Santos, F. P., Chuss, D. T., Dowell, C. D., et al. 2019, *ApJ*, 882, 113, doi: [10.3847/1538-4357/ab3407](https://doi.org/10.3847/1538-4357/ab3407)
- Sarkar, A., Looney, L. W., Pound, M. W., et al. 2025, *Magnetic Fields in the Pillars of Creation*. <https://arxiv.org/abs/2506.14902>
- Schisano, E., Rygl, K. L. J., Molinari, S., et al. 2014, *The Astrophysical Journal*, 791, 27, doi: [10.1088/0004-637X/791/1/27](https://doi.org/10.1088/0004-637X/791/1/27)
- Seifried, D., Walch, S., & Balduin, T. 2025, *MNRAS*, 542, 3302, doi: [10.1093/mnras/staf1423](https://doi.org/10.1093/mnras/staf1423)
- Seo, Y. M., Dowell, C. D., Goldsmith, P. F., Pineda, J. L., & Majumdar, L. 2021, *ApJ*, 917, 57, doi: [10.3847/1538-4357/ac0c80](https://doi.org/10.3847/1538-4357/ac0c80)
- Shetty, R., Kauffmann, J., Schnee, S., & Goodman, A. A. 2009, *ApJ*, 696, 676, doi: [10.1088/0004-637X/696/1/676](https://doi.org/10.1088/0004-637X/696/1/676)
- Stephens, I. W., Looney, L. W., Dowell, C. D., Vaillancourt, J. E., & Tassis, K. 2011, *ApJ*, 728, 99, doi: [10.1088/0004-637X/728/2/99](https://doi.org/10.1088/0004-637X/728/2/99)
- Stephens, I. W., Coudé, S., Myers, P. C., et al. 2025, *ApJ*, 995, 181, doi: [10.3847/1538-4357/ac08a8](https://doi.org/10.3847/1538-4357/ac08a8)
- Tram, Le Ngoc, Hoang, Thiem, Wiesemeyer, Helmut, et al. 2024, *A&A*, 689, A290, doi: [10.1051/0004-6361/202450127](https://doi.org/10.1051/0004-6361/202450127)
- Trapman, L., Rosotti, G., Zhang, K., & Tabone, B. 2023, *The Astrophysical Journal*, 954, 41, doi: [10.3847/1538-4357/ace7d1](https://doi.org/10.3847/1538-4357/ace7d1)
- Vaillancourt, J. E. 2002, *ApJS*, 142, 53, doi: [10.1086/341398](https://doi.org/10.1086/341398)
- Vazzano, M. M., Cappa, C. E., Vasquez, J., Rubio, M., & Romero, G. A. 2014, *A&A*, 570, A109, doi: [10.1051/0004-6361/201423369](https://doi.org/10.1051/0004-6361/201423369)
- Virtanen, P., Gommers, R., Oliphant, T. E., et al. 2020, *Nature Methods*, 17, 261, doi: [10.1038/s41592-019-0686-2](https://doi.org/10.1038/s41592-019-0686-2)
- Wu, Y. W., Sato, M., Reid, M. J., et al. 2014, *A&A*, 566, A17, doi: [10.1051/0004-6361/201322765](https://doi.org/10.1051/0004-6361/201322765)
- Zielinski, N., & Wolf, S. 2022, *A&A*, 659, A22, doi: [10.1051/0004-6361/202141537](https://doi.org/10.1051/0004-6361/202141537)
- Zucker, C., Schlafly, E. F., Speagle, J. S., et al. 2018, *The Astrophysical Journal*, 869, 83, doi: [10.3847/1538-4357/aae97c](https://doi.org/10.3847/1538-4357/aae97c)
- Zucker, C., Speagle, J. S., Schlafly, E. F., et al. 2020, *A&A*, 633, A51, doi: [10.1051/0004-6361/201936145](https://doi.org/10.1051/0004-6361/201936145)
- Zuckerman, B., & Evans, II, N. J. 1974, *ApJL*, 192, L149, doi: [10.1086/181613](https://doi.org/10.1086/181613)

Region	Band	Plan ID	PI	Exposure (s)	Chop Angle (°)	Chop Amp (")	Pipeline Version	Original Reference
L1527	D	70.0609	GTO	2251.9	-75	210	3.2.0	This Paper
L1688	A	70.0609	GTO	4730.6	30	240	3.2.0	This Paper
L1688	C	70.0511, 70.0609	GTO	3842.3	30	240	3.2.0	Santos et al. (2019)
L1688	D	70.0511	GTO	833.5	30	240	3.2.0	Santos et al. (2019)
ρ Oph E/F	D	05.0133, 06.0116	Giles Novak	2773.6	-72	240	3.2.0	Lee et al. (2021) , This Paper
L1689N	C	07.0147	Giles Novak	1213.7	-85	200	3.2.0	Encalada et al. (2024)
L1689N	D	06.0116	Giles Novak	321.6	-85	210	3.2.0	Encalada et al. (2024)
NGC 1333	C	05.0081, 06.0099	Fabio Santos	5053.7	-108	240	3.2.0	This Paper
NGC 1333	E	06.0098	Ian Stephens	3595.9	90	250	3.2.0	This Paper
OMC1	A	70.0609, 70.0509	GTO	5762.3	125	230	1.3.0beta3	Chuss et al. (2019)
OMC1	C	88.0005, 70.0509	GTO	3697.7	-55	240	1.3.0beta3	Chuss et al. (2019)
OMC1	D	70.0509	GTO	756.8	125	230	1.3.0beta3	Chuss et al. (2019)
OMC1	E	70.0509	GTO	1034.8	125	230	1.3.0beta3	Chuss et al. (2019)
OMC2/3	D	07.0026, 07.0237	Stefan Heese, Joseph Michail	3218.1	-90	250	2.7.0	Zielinski & Wolf (2022) , This Paper
OMC2/3	E	07.0026	Stefan Heese	2876.9	90	250	3.2.0	Zielinski & Wolf (2022)
NGC 2071	E	06.0119	Ian Stephens	2063.6	15	250	3.2.0	This Paper
NGC 2068	E	06.0119	Ian Stephens	1492.1	45	250	3.2.0	This Paper
Serpens	E	05.0206, 06.0088, 06.0180, 07.0238	Thushara Pillai, Paul Goldsmith	10159.2	-50	150	3.2.0	Pillai et al. (2020)
Vela C	C	70.0609	GTO	1661.3	-67.5	240	3.2.0	Bij et al. (2024)
Vela C	E	70.0609	GTO	946.7	-67.5	240	3.2.0	Bij et al. (2024)
S106	A	06.0014	Dan Clemens	653.6	-60	250	2.7.0	This Paper
S106	E	06.0014	Dan Clemens	474.6	-60	250	2.7.0	This Paper
NGC 6334	A	70.0609	GTO	1772.9	-135	210	3.2.0	This Paper
NGC 6334	C	70.0609	GTO	472.1	-135	210	3.2.0	This Paper
NGC 6334	D	70.0609	GTO	465.7	-135	210	3.2.0	This Paper
NGC 6334	E	70.0609	GTO	472.1	-135	210	3.2.0	This Paper
DR21	A	06.0014, 07.0013	Dan Clemens	3902.9	-110	190	2.7.0	This Paper
DR21	E	06.0014, 07.0013	Dan Clemens	3379.0	-110	250	2.7.0	This Paper
G34.43	E	06.0039	Dan Clemens	1728.6	-110	200	3.2.0	This Paper
M17	A	70.0609	GTO	908.3	-100	225	3.2.0	This Paper
M17	C	70.0609	GTO	2332.6	-100	225	3.2.0	Cox et al. (2025)
M17	D	70.0609	GTO	1530.0	0	150	3.2.0	Hoang et al. (2022)
M17	E	70.0609	GTO	710.2	-100	225	3.2.0	Cox et al. (2025)
G14.2N	D	06.0183, 07.0066	Fabio Santos	1621.4	-95	240	2.7.0	This Paper
G14.2S	D	06.0183	Fabio Santos	892.09	40	240	3.2.0	This Paper
M16	C	06.0059	Marc Pound	3367.7	-78	250	3.2.0	Sarkar et al. (2025)
M16	D	05.0112	Marc Pound	1332.3	-82.7	250	3.2.0	Sarkar et al. (2025)
G351.77	E	07.0238	Thushara Pillai	1302.3	140	250	2.7.0	This Paper
W3OH	A	90.0084, 70.0509	GTO	1000.7	-70	219	2.7.0	This Paper
W3OH	C	70.0509	GTO	919.1	-85	225	2.7.0	This Paper
W3OH	D	90.0084	GTO	446.0	-75	233	2.7.0	This Paper
W3OH	E	70.0509	GTO	1471.3	-85	225	2.7.0	This Paper

W3	A	90.0084, 05_0038	GTO, John Vaillancourt	2373.2	-70	219	2.7.0	This Paper
W3	C	90.0084	GTO	1176.3	-70	219	2.7.0	Cox et al. (2025)
W3	D	88.0005, 90_0084	GTO	1681.8	-75	233	2.7.0	Cox et al. (2025)
W3	E	90.0084	GTO	2324.0	-75	233	2.7.0	Cox et al. (2025)
W33	A	05_0038	John Vaillancourt	839.0	35	250	3.2.0	This Paper
W33	C	05_0038	John Vaillancourt	306.4	30	219	3.2.0	This Paper
W33	E	05_0038	John Vaillancourt	422.9	25	250	3.2.0	This Paper
BYF77	D	07_0089	Peter Barnes	1117.8	-20	250	3.2.0	Barnes et al. (2025)
BYF73	D	07_0089	Peter Barnes	784.4	-65	250	3.2.0	Barnes et al. (2023)
Keyhole	C	07_0081	Darren Dowell	10303.2	-5	210	3.2.0	Seo et al. (2021)

Table A.1. A table of every HAWC+ dataset used in our compilation. The last column lists the reference for the first publication of the data. For the datasets that list our paper and another paper, a portion of the data was published but we have included more observations. Entries in the Original Reference column that include a different paper and the text "This Paper" use a dataset that is a combination of previously published data and additional data from the archive.